Realia et naturalia

DISSERTATIONES
CHIMICAE
UNIVERSITATIS
TARTUENSIS
131

KADI TAMM

Synthesis and characterization of the micro-mesoporous anode materials and testing of the medium temperature solid oxide fuel cell single cells

TARTU ÜLIKOOL
1632
UNIVERSITAS TARTUENSIS

DISSERTATIONES CHIMICAE UNIVERSITATIS TARTUENSIS
131

DISSERTATIONES CHIMICAE UNIVERSITATIS TARTUENSIS
131

KADI TAMM

Synthesis and characterization of the micro-mesoporous anode materials and testing of the medium temperature solid oxide fuel cell single cells

UNIVERSITY OF TARTU
PRESS
1632

Institute of Chemistry, Faculty of Science and Technolog, University of Tartu, Estonia

Dissertation is accepted fot the commencement of the degree of Doctor of Philosophy in Chemistry on November 08, 2013 by the Council of Institute of Chemistry, University of Tartu.

Supervisor: Prof. Enn Lust
University of Tartu, Estonia

Opponent: Prof. Peter Holtappels
Technical University of Denmark, Denmark

Commencement: 19.12.2013, at 12:00. Auditorium 1021, Ravila 14a, Tartu

ISSN 1406–0299
ISBN 978–9949–32–455–2 (print)
ISBN 978–9949–32–456–9 (pdf)

University of Tartu Press
www.tyk.ee

TABLE OF CONTENTS

1. LIST OF ORIGINAL PUBLICATIONS 7
2. ABBREVATIONS AND SYMBOLS 8
3. INTRODUCTION 10
4. LITERATURE OVERVIEW 12
   - 4.1. Design of solid oxide fuel cell single cells 12
     - 4.1.1. Ni-cermet anodes 13
     - 4.1.2. Ceramic perovskite oxide anodes 15
   - 4.2. Microstructure of the anode 17
     - 4.2.1. Electrode fabrication by applying infiltration method 19
   - 4.3. Electrochemical reactions in SOFC electrodes 20
   - 4.4. Methods for electrochemical characterization of SOFCs properties 23
     - 4.4.1. Cyclic voltammetry 23
     - 4.4.2. Electrochemical impedance spectroscopy 24
     - 4.4.3. Alternative analysis of impedance spectra 25
     - 4.4.4. Fitting of impedance data 27
5. EXPERIMENTAL 29
   - 5.1. Single cell preparation 29
     - 5.1.1. Preparation of the electrolyte supported Ni-GDC10|GDC10|LSC40 29
     - 5.1.2. Preparation of the anode supported Ni-GDC10|ScSZ6-GDC10|LSC40 30
     - 5.1.3. Preparation of the electrolyte supported LSV30-SDC15|SDC15|SDC15-LSC20 32
   - 5.2. Experimental measurement setups and physical characterization of the electrode materials 34
6. RESULT AND DISCUSSION 37
   - 6.1. Electrochemical impedance spectroscopy [Papers I–IV] 37
     - 6.1.1. Analysis of impedance spectra [Papers I, II, IV] 43
   - 6.2. Influence of the supportive Ni-GDC cermet anode microstructure on the SOFC single cell performance [Papers II, IV] 47
   - 6.3. Influence of the ceramic LSV30-SDC15 anode microstructure on the SOFC single cell performance [Papers III, V] 52
     - 6.3.1. Influence of the SDC matrix surface area on the electrochemical performance of the single cell [Paper III] 58
     - 6.3.2. Influence of the SDC matrix porosity and pore size on the electrochemical performance of the single cell [Paper V] 60

7. SUMMARY 63
8. REFERENCES 64
9. SUMMARY IN ESTONIAN 68
10. ACKNOWLEDGEMENTS 69
11. PUBLICATIONS 71
CURRICULUM VITAE 128

I. LIST OF ORIGINAL PUBLICATIONS

I. E. Lust, R. Küngas, I. Kivi, H. Kurig, P. Möller, E. Anderson, K. Lust, **K. Tamm**, A. Samusshenko, G. Nurk, Electrochemical and gas phase parameters of cathodes for intermediate temperature solid oxide fuel cells. Electrochimica Acta, 55 (26) (2010) 7669–7678.

II. **K. Tamm**, I. Kivi, E. Anderson, P. Möller, G. Nurk, E. Lust, Influence of graphite pore forming agents on the structural and electrochemical properties of porous Ni-CGO anode. Journal of the Electrochemical Society, 159 (12) (2012) F849–F857.

III. **K. Tamm**, R. Küngas, R.J. Gorte, E. Lust, Solid oxide fuel cell anodes prepared by infiltration of strontium doped lanthanum vanadate into doped ceria electrolyte. Electrochimica Acta, 106 (2013) 398–405.

IV. **K. Tamm**, I. Kivi, E. Anderson, P. Möller, G. Nurk, E. Lust, Optimization of solid oxide fuel cell Ni-CGO anode porosity. ECS Transaction, 35 (1) (2011) 1771–1779.

V. **K. Tamm**, R. Raudsepp, R. Kanarbik, P. Möller, G. Nurk, E. Lust, Investigation of microstructure of Sr-doped lanthanum vanadium oxide anode based on SDC electrolyte. ECS Transaction, 57(1) (2013) 1185–1191.

Author's contribution:

Paper I: Participated in the synthesis and electrochemical characterization of the single cells.

Paper II: Performed the synthesis of the single cells, some physical and all electrochemical characterization of the single cells and analysis of the data. Mainly responsible for the preparation of the manuscript.

Paper III: Performed the synthesis of the single cells, some physical and all electrochemical characterization of the single cells and analysis of the data. Mainly responsible for the preparation of the manuscript.

Paper VI: Performed the synthesis of the single cells, some physical and all electrochemical characterization of the single cells and analysis of the data. Mainly responsible for the preparation of the manuscript.

Paper V: Performed the synthesis of the single cells, some physical and all electrochemical characterization of the single cells and analysis of the data. Mainly responsible for the preparation of the manuscript.

2. ABBREVATIONS AND SYMBOLS

$\Delta\partial Z_{anodic}$	–	difference between the derivatives of the spectrums obtained at different hydrogen partial pressures
$\Delta\partial Z_{cathodic}$	–	difference between the derivatives of the spectrums obtained at different oxygen partial pressures
$\Delta\partial Z_{potential}$	–	difference between the derivatives of the spectrums obtained at different cell potentials
AC	–	alternating current
ADIS	–	analysis of differences in impedance spectra
AS	–	anode supported
BET method	–	Brunauer-Emmett-Teller method
C	–	capacitance
GDC	–	$Ce_{1-x}Gd_xO_{2-\delta}$
GDC10	–	$Ce_{0.9}Gd_{0.1}O_{2-\delta}$
CPE	–	constant phase element
CV	–	cyclic voltammetry
DPB	–	double-phase boundary
d_{pore}	–	pore diameter
E	–	potential
EC	–	equivalent circuit
E_{fix}	–	fixed single cell potential
EIS	–	electrochemical impedance spectroscopy
E_{N}	–	maximal theoretical cell potential; Nernst potential
ES	–	electrolyte supported
F	–	Faraday constant
f	–	frequency
FIB	–	focused ion beam
f_{max}	–	characteristic frequency
f_{max1}	–	characteristic frequency of the first semicircle
f_{max2}	–	characteristic frequency of the second semicircle
f_{max3}	–	characteristic frequency of the third semicircle
i	–	imaginary unit
$I(t)$	–	ac current function; subsequent current
I_0	–	current amplitude
IT	–	intermediate temperature
j	–	current density
L	–	high frequency inductance
LSC	–	$La_{1-x}Sr_xCoO_{3-\delta}$
LSC20	–	$La_{0.8}Sr_{0.2}CoO_{3-\delta}$
LSC40	–	$La_{0.6}Sr_{0.4}CoO_{3-\delta}$
LSCF	–	$La_{1-x}Sr_xCo_{1-y}Fe_yO_{3-\delta}$
LSF	–	$La_{1-x}Sr_xFeO_{3-\delta}$
LSGM	–	$La_{1-x}Sr_xGa_{1-y}Mn_yO_{3-\delta}$

LSM – $La_xSr_{1-x}MnO_{3-\delta}$
LST – $La_xSr_{1-x}TiO_{3-\delta}$
LSV – $La_{1-x}Sr_xVO_{3-\delta}$
LSV30 – $La_{0.7}Sr_{0.3}VO_{3-\delta}$
MIEC – mixed ionic and electronic conductor
OCV – open circuit voltage
P – power density
P_{max} – maximum power density
PMMA – polymethyl methacrylate
P_{O2} – the partial pressure of oxygen at the electrode
P_{tot} – total pore volume
PVF – pore volume fraction
R – gas constant
R – characteristic resistances of the semicircles
R_1 – resistance of the first semicircle
R_2 – resistance of the second semicircle
R_3 – resistance of the third semicircle
R_P – polarization resistance
R_s – high-frequency series resistance
R_{tot} – total resistance
R_Ω – ohmic resistance
S_{BET} – specific surface area frim BET analysis
ScSZ – $Zr_{1-x}Sc_xO_{2-\delta}$
ScSZ6 – $Zr_{0.94}Sc_{0.06}O_{2-\delta}$
SDC – $Ce_{1-x}Sm_xO_{2-\delta}$
SDC15 – $Ce_{0.85}Sm_{0.15}O_{2-\delta}$
SEM – scanning electron microscopy
SOFC – solid oxide fuel cell
T – temperature
t – time
TPB – thee phase boundary
$U(t)$ – ac potential function
U_0 – steady-state potential
W – short circuit Warburg impedance
YSZ – $Zr_{1-x}Y_xO_{2-\delta}$
YSZ8 – $Zr_{0.92}Y_{0.08}O_{2-\delta}$
$Z(t)$ – impedance as a function of time
$Z(\omega)$ – impedance as a function of angular frequency
Z' – real part of impedance
Z'' – imaginary part of impedance
ρ – density
ρ_0 – theoretical density
φ – phase shift between potential and current
ω – angular frequency

3. INTRODUCTION

Solid oxide fuel cells (SOFC) are being considered to be the promising energy conversion systems due to their high electrical efficiency (up to 60%), fuel flexibility (CH_4, CH_3OH, C_2H_5OH, etc) and environmental friendliness [1–4]. Depending on the fuel composition and the working temperature, the total chemical energy conversion efficiency into electricity and heat together can be even up to 85% [3,5,6].

The most commonly used SOFC single cell consists of yttria-stabilized zirconia, $Zr_{1-x}Y_xO_{2-\delta}$ (YSZ), electrolyte, Ni-YSZ composite anode and $La_xSr_{1-x}MnO_{3-\delta}$ (LSM)-YSZ composite cathode working effectively at the temperatures from 973 to 1273 K. The main advantage of these materials selection is relatively low reactivity of YSZ with NiO, as well as with LSM, making the fabrication of the single cells very simple [7]. However, these materials have also remarkable disadvantages, main ones being high materials cost and limited long-term stability. Both of these problems can be solved by lowering the working temperature and using the so-called intermediate temperature (IT) (773–973 K) SOFC concept. Lowering the working temperature enhances the long-term stability and widens the SOFCs construction materials selection, including the suitable sealing materials. There are two different approaches in lowering the working temperature: *(i)* design and development of new materials, and *(ii)* optimization of the electrode microstructures.

YSZ has quite poor ionic conductivity at temperatures below 873 K. For IT-SOFC concept the alternative electrolyte materials, such as gadolinia doped ceria, $Ce_{1-x}Gd_xO_{2-\delta}$ (GDC), or samaria doped ceria, $Ce_{1-x}Sm_xO_{2-\delta}$ (SDC), are being used for acceptable electrochemical performance [8,9]. However, the selection of anode and cathode, i.e. electrode materials, is partially determined by the chemical composition of electrolyte [5,7].

Oxygen reduction is considered to be the rate limiting step for SOFC performance and therefore due to its low catalytic activity at IT region the LSM is not suitable cathode material at these conditions [10]. Various authors have demonstrated that one of the suitable cathode material for IT-SOFC is $La_xSr_{x-1}CoO_{3-\delta}$, [9,11–18], a mixed electronic and ionic conductor with ABO_3 perovskite structure.

Ni is a suitable electronically conductive and catalytically active material for IT-SOFC anode. However, to achieve the suitable maximal power densities at the anode, the fuel electrode must have sufficient porosity to allow the fuel transport to the reaction sites and byproduct(s) away from the reaction sites. Optimization of the Ni-cermet anode|electrolyte half-cell structure is important to guarantee quick supply of oxide ions from cathode to anode, thus an adequate electronic conductivity of the anode [3,19]. Ni-cermet composite is a perfect anode material if hydrogen is being used as a fuel. However, Ni-cermet anode suffers from severe deactivation in hydrocarbon and hydrocarbon derived fuels. The deactivation is mainly caused by the extensive cocking (carbon deposition)

onto the Ni-cermet surface [20–25]. Ni-cermet poisoning with sulfur, a result of the fuel impurities, is another issue that still needs to be solved [26–29].

Promising alternatives to the Ni-cermet anodes in SOFCs are anodes based on the ceramic conductors with the perovskite structure, for example $La_{1-x}Sr_xCr_{1-y}Mn_yO_{3-\delta}$ or $La_{1-x}Sr_xTiO_{3-\delta}$ [25,30,31]. It has been shown that because of the relatively low catalytic activity, ceramic anodes are much more tolerant toward the carbon deposition and sulfur poisoning than Ni-cermet anodes [19]. However, to achieve the reasonable electrochemical activity of the ceramic anodes, the additional catalysts (catalytic centers), like CeO_2 and Pd, must be deposited into the anode [30,31].

Lately, the doped rare-earth vanadates have been shown to exhibit sufficient conductivity, at least for use as the anode functional layer. For instance, the electronic conductivity of a composite electrode consisting of $La_{1-x}Sr_xVO_{3-\delta}$ (LSV) infiltrated into YSZ porous scaffold has been reported to be greater than 2 S cm^{-1} at 973 K [32]. Like for Ni-cermet anodes, the microstructure of the ceramic anodes is crucial to the desirable performance of SOFC. Therefore the influence of the microstructure on the ceramic anode has to be investigated in detail.

The main aim of this work was to prepare and analyze the electrochemical performance of the IT-SOFCs single cells based on the Ni-cermet and LSV-cermet anode and GDC or SDC electrolyte (i.e. ionic conductor). Second very important aim was to investigate the influence of the microstructure of the anodes on the electrochemical characteristics of the SOFC single cells. The detailed analysis of the electrochemical and physical data has been carried out.

4. LITERATURE OVERVIEW

4.1. Design of solid oxide fuel cell single cells

Solid oxide fuel cell (SOFC) is an energy conversion device that directly converts chemical energy, contained in the chemical bonds of the fuel, into electrical energy. SOFC single cell consists of oxide ion conducting material(s) as an electrolyte, sandwiched between the porous electrodes: (*i*) cathode, where the oxygen reduction takes place, and (*ii*) anode, where the oxidation of fuels takes place. SOFC is especially attractive because of its relatively high efficiency, environmental friendliness and fuel flexibility (in comparison with polymer electrolyte membrane fuel cell). The electrical efficiency of SOFC can be up to 60% [1,2,4,5] and by using the residual heat generated during the exothermal fuel electrooxidation reaction the total chemical energy conversion efficiency into electricity and heat together can be expected to be up to 85% [3,6]. SOFC can operate with zero CO_2 emission if H_2 is used as a fuel, and without production of undesirable gases, such as NO_x and SO_x [5]. In principle, SOFC can operate on any combustible fuel, including natural gas, liquid hydrocarbons (hexane, n-butane, n-decane), and even solid powdered fuels derived from coal or biomass [19,33].

One of the most common designs for SOFCs is the planar design. It consists of the series of cell components configured as thin flat plates electrically connected through the current collectors into stacks to build up systems with desirable electrochemical performance. The planar design is simpler, less expensive to manufacture and has higher power densities than the tubular design [7]. However, this design requires high-temperature gastight seals between the cell components [4,7,34]. The traditional planar SOFC configuration has a thick electrolyte layer as a supportive construction element. Because of that, the performance of the cell decreases remarkably due to high energetic losses in the thick electrolyte. The technological advances in the ceramic processing (screen printing, tape casting, slurry sintering or plasma spraying) has made it possible to prepare very thin electrolyte layers. As a result, an anode supported planar SOFC design has been developed [7].

For intermediate temperature (IT)-SOFC, doped $LaGaO_3$ and doped CeO_2 have been found to be the suitable electrolyte materials instead of traditional $Zr_{1-x}Y_xO_{2-\delta}$ (YSZ) electrolyte [8,10]. $La_{1-x}Sr_xGa_{1-y}Mn_yO_{3-\delta}$ (LSGM) is a promising alternative electrolyte material with relatively high conductivity, 0.11–0.14 S cm^{-1} at 1073 K and 0.02–0.04 S cm^{-1} at 773 K (depending on the doping level, i.e. on the x and y values) [8,9]. For comparison, conductivities for $Zr_{0.92}Y_{0.08}O_{2-\delta}$ (YSZ8) are 0.1 S cm^{-1} at 1073 K and 0.004 S cm^{-1} at 873 K, respectively [6,8]. However, LSGM has some disadvantages, like possible reduction and volatilization of gallium oxide, formation of stable secondary phase in the course of processing, the relatively high cost of gallium and significant reactivity with ceramic perovskite electrodes under oxidation

condition and metal-cermet anodes in fuel oxidation conditions [8]. The most studied and attractive doped CeO_2 electrolytes are $Ce_{1-x}Gd_xO_{2-\delta}$ (GDC) and $Ce_{1-x}Sm_xO_{2-\delta}$ (SDC). The main advantage of GDC and SDC is the higher ionic conductivity, particularly at lower temperatures (0.013 S cm^{-1} and 0.019 S cm^{-1} at 873 K for GDC and SDC, respectively [8]), with respect to YSZ8 electrolyte, and the lower cost in comparison with LSGM and its derivate.

The main problem for using the doped ceria as a SOFC electrolyte is the partial reduction of Ce^{4+} to Ce^{3+} under the reducing conditions [3,8]. This has two main effects: (*i*) the n-type electronic conductivity will appear causing the partial internal electronic short circuit of a cell, and (*ii*) some nonstoichiometry and expansion of the electrolyte lattice takes place leading to the mechanical failure of the anode|electrolyte or cathode|electrolyte interface. The second effect can be eliminated via working in IT region. However, the partial electronic conductivity of the electrolyte reduces the open circuit voltage (OCV) resulting in somewhat lower electrical efficiency of the SOFC single cells. Some studies have shown that the electronic conductivity is influenced by temperature, electrolyte thickness, electrode polarization resistance and fuel utilization rate, i.e. the current density of a cell [8]. Taking also into account that doped ceria is relatively unreactive towards potential IT electrode materials, in particular with cobalt-based cathode materials ($La_{1-x}Sr_xCoO_{3-\delta}$ (LSC), $La_{1-x}Sr_xCo_{1-y}Fe_yO_{3-\delta}$ (LSCF), etc.), it seems to be a very suitable electrolyte material especially for IT-SOFC.

For IT-SOFC cathode alternative materials to $La_{1-x}Sr_xMnO_{3-\delta}$ (LSM)-YSZ composites have been developed because LSM has low ionic conductivity at IT region [10]. Desirable cathode materials for IT-SOFC are considered to be mixed ionic and electronic conductors (MIEC), such as perovskite type oxides like $La_{1-x}Sr_xCoO_3$ (LSC), $La_{1-x}Sr_xFeO_3$ (LSF) or $La_{1-x}Sr_xCo_{1-y}Fe_yO_3$ (LSCF) [9,11–16,18,35,36]. However, the preparation of these alternative electrodes can be complicated because many mixed conducting perovskites undergo a solid-state reaction with YSZ at the sintering temperature used for preparation of traditional SOFC electrodes (mainly cathodes). This problem can be solved by using a ceria based barrier layer between YSZ electrolyte and active cobaltite cathode [13,17,18] or replacing an zirconium based electrolyte entirely with cerium based compound [11,14,36].

4.1.1. Ni-cermet anodes

Current state of art anode materials for SOFC are based on Ni-cermet composites where porous Ni structures ensure the electronic conductivity and the dense electrolyte, most commonly YSZ, ensures the ionic conductivity of an anode [19]. In addition, Ni is also a very good catalyst for hydrogen oxidation as well for the steam reforming of methane to produce the syn gas. The most commonly used method for producing the Ni-cermet anodes is mixing of the NiO and the electrolyte powders. These Ni-cermet powders can be screen

printed onto the supporting electrolytes (for the electrolyte supported (ES) cells), or these mixtures can be used for preparation of plates by pressing or tape-casting (for the anode supported (AS) configuration) [3,19].

Currently, the SOFC Ni-cermet anode is mostly fabricated using tape casting method to make thick supportive anode, thin functional anode and thin electrolyte layer(s). These layers are later laminated and co-sintered, and followed by preparation of the cathode [37]. For example, Ding and Hashida [38] constructed a Ni-GDC anode supported SOFC with a thin $Ce_{0.9}Gd_{0.1}O_{2-\delta}$ (GDC10) electrolyte film (fabricated by spray drying and co-pressing method) and nanostructured LSCF cathode (prepared by sol-gel and screen-printing method). This SOFC single cell showed high electrochemical performance at low operating temperatures, the maximum power density, P_{max}, values in the case of H_2 fuel were 297 mW cm^{-2} at 773 K and 992 mW cm^{-2} at 873 K.

The Ni-cermet anodes have already become quite mature for SOFCs and are currently used as anode electron conductive material in commercially available high temperature SOFC small power generation systems in Japan [39]. From the long-term studies a lot is known how Ni-cermet anode behaves under various application conditions, therefore a lot is known for its shortcomings compared to alternative ceramic anode materials. However, there is still a lot to investigate, especially in identifying the width of reaction zones, to better design optimal cermet microstructures and optimal chemical composition influencing the three-phase boundary characteristics in terms of activity and durability [7]. Typical polarization resistance values for the Ni-YSZ-cermet anode, operating with humidified hydrogen, reported by the leading SOFC developers are in the range of 0.02–0.06 Ω cm^2 at 1273 K, 0.04–0.08 Ω cm^2 at 1123 K and 0.06–0.10 Ω cm^2 at 1023 K, respectively [7,40,41].

Unfortunately, Ni-cermet anodes have some serious drawbacks [19]. Firstly, metallic Ni centers catalyze the formation of carbon filaments, if hydrocarbon fuels are being used, leading to extensive cocking of the anode [20–25,42]. Hydrocarbons can also react in the gas phase via free-radical cracking and polymerization, forming tars that can then deposit onto the anode surfaces [19]. Carbon deposition can be somewhat suppressed by feeding the large excess of steam into the system. Secondly, poor redox stability is also a problem for Ni-cermet anodes. Ni can become oxidized back into NiO at high oxygen partial pressures and during shut down periods, causing the microstructural changes in the metal-cermet composite anode [19,43,44]. Thirdly, the low tolerance of Ni-cermet anodes towards fuel impurities, including sulfur containing compounds, remains a largely unsolved problem [26–29]. Sulfur concentration as low as 1 ppm in the fuel already causes significant degradation of the performance of Ni-YSZ anodes [28,29]. However, there are three main trends in approaching these problems in the research: (*i*) enhancing the performance of Ni-cermet anodes, (*ii*) replacing Ni with other metallic materials such as Cu, and (*iii*) using the conductive ceramics to replace metal matrix in the metal-cermet anode [33].

4.1.2. Ceramic perovskite oxide anodes

In ceramic oxide anodes with perovskite structures the electron transport is provided by the ceramic components rather than by the metal network. The general idea to apply the ceramic anodes is that since the metal components of the anode are the ones that exhibit very low tolerance towards hydrocarbons (carbon deposition) and other impurities (like sulfur), these problems can be eliminated by removing the metal network altogether and exploring only the ceramic components for electron transport and electrocatalysis. Ideally a mixed ionic and electronic conducting (MIEC) ceramics are being used [33]. Metal oxides tend to be poor reforming catalysts and unlikely to form carbon fibers while using the hydrocarbon fuels [19]. The electronic conductivity of the ceramic anode also needs to be maintained over both reducing and oxidizing conditions in order to allow operation at both very low and high fuel utilizations [33]. Materials that have the compromise of the redox stability and high electronic conductivity are considered to be the perovskite type ABO_3 oxides in which more than one cation is used on the A and/or B sites [24,33].

One very widely studied B site cation for ceramic anodes is Ti. However, strontium titanate, $SrTiO_3$, is a good electron conductor only at low oxygen partial pressures. For the application as an SOFC anode $SrTiO_3$ is doped to increase the electronic conductivity. For example yttrium, niobium and lanthanum are being used as A-position dopants [25,45]. The conductivity of lanthanum-strontium titanate, $La_xSr_{1-x}TiO_{3-\delta}$ (LST) generally increases with lanthanum concentration and appears to level off at a lanthanum content of around 0.4 [25].

Lee et al [31] measured the maximum conductivity of 2 S cm^{-1} at 973 K in humidified (3% H_2O) H_2 for 45 wt% $La_{0.3}Sr_{0.7}TiO_{3-\delta}$ infiltrated into YSZ8 porous scaffold followed by heating at 1373 K. The maximum power density of 20 mW cm^{-2} for the single cell with LSF cathode was recorded at 1073 K in the case of humidified H_2. However, P_{max} increased to 1100 mW cm^{-2} if the catalytically active centers of Pd and ceria were added into the $La_{0.3}Sr_{0.7}TiO_{3-\delta}$-YSZ8 anode. The value of polarization resistance, R_P, for the catalytically activated SOFC single cell was 0.5 Ω cm^{-2} at 973 K in the case ofhumidified H_2 [31]. Yoo and Choi [46] reported P_{max} of 67 mW cm^{-2} at 1073 K for $La_{0.2}Sr_{0.8}TiO_{3-\delta}$-GDC10 cermet anode system ($LaGaO_3$-cermet electrolyte and LSCF cathode were used) in humidified H_2 fuel. Some increase in the cell performance was established after adding small amounts of Ni centers into the anode, P_{max} increased to 300 mW cm^{-2} and R_P decreased to 0.95 Ω cm^2 [46]. Hussain et al [47] improved the $Sr_{0.94}Ti_{0.9}Nb_{0.1}O_3$ anode performance by adding a metal functional layer and also activating the anode with Pd naonparticles. As a result, R_P decreased from 90 Ω cm^2 to 30 Ω cm^2 and to 0.35 Ω cm^2, respectively, at 873 K and in the case of humidified H_2.

Chromium is another element commonly used for B site metal. $LaCrO_3$ is a stable perovskite. After doping $LaCrO_3$ with calcium or strontium, it is the most

common ceramic interconnect material for SOFC [25]. It is well-known that the catalytic activity of the perovskite oxide is the highest when the oxide-ion conductivity is high, so the B-site of strontium-doped $LaCrO_3$ is being commonly doped with various transition metals (Mn, Fe, Co, Ni, Cu) to create the oxygen vacancies.

Tao and Irvine investigated $La_{0.75}Sr_{0.25}Cr_{0.5}Fe_{0.5}O_{3-\delta}$ [48] as well as $La_{0.75}Sr_{0.25}Cr_{0.5}Mn_{0.5}O_{3-\delta}$ [30] as the potential anode materials. For $La_{0.75}Sr_{0.25}Cr_{0.5}Fe_{0.5}O_{3-\delta}$ anode consisting SOFC single cell the values of R_P 1.15 Ω cm^2 in humidified H_2 and 1.75 Ω cm^2 in humidified methane were measured at 1123 K [48]. However, for $La_{0.75}Sr_{0.25}Cr_{0.5}M_{0.5}O_{3-\delta}$ anode the value of R_P 0.6 Ω cm^2 and P_{max} 300 mW cm^{-2} were measured at 1123 K and in humidified H_2 [30]. Liu et al [49] mixed $La_{0.8}Sr_{0.2}Cr_{0.5}Mn_{0.5}O_{3-\delta}$ electronic conductor with GDC (typical IT electrolyte material) to improve the ionic conductivity of the anode by increasing the concentration of the three-phase boundaries, and added small amount of nanoscale NiO particles to increase the catalytic activity. $La_{0.8}Sr_{0.2}Cr_{0.5}Mn_{0.5}O_{3-\delta}$-GDC-Ni anode had comparable power densities with Ni-GDC anode, ~150 mW cm^{-2}, at 1023 K in H_2 atmosphere. However, working in propane atmosphere, the ceramic anode had surprisingly larger power density than Ni-cermet anode containing SOFC single cell.

Kim et al [50] prepared the SOFC single cell by impregnation of nitrate salts into raw anodes to produce the composites with 45 wt% $La_{0.8}Sr_{0.2}Cr_{0.5}Mn_{0.5}O_{3-\delta}$ in a 65% porous YSZ8 scaffold. Composites prepared in this manner exhibited at 1073 K conductivities of ~1 S cm^{-1} in air and 0.1 S cm^{-1} in humidified H_2, respectively. The value of maximum power density 50 mW cm^{-2} was established for composite anode at 973 K in humidified H_2. However, P_{max} increased to 520 mW cm^{-2} if 0.5 wt% Pd and 5 wt% ceria were added into the anode as catalysts.

Madsen and Barnett [51] doped chromium center (B position) with vanadium, $La_{0.8}Sr_{0.2}Cr_{0.98}V_{0.02}O_{3-\delta}$, and added GDC and small amounts of NiO. They reported the single cell performance in various fuels, H_2, CH_4, C_2H_6, C_3H_8 and C_4H_{10}. At 973 K in H_2, P_{max} was 97 mW cm^{-2} and R_P 0.9 Ω cm^2. Remarkably better single cell performance and stability in hydrocarbon fuels were reported than for Ni-cermet anode consisting single cells. Authors believed the cell performance could be improved even more by modifying the anode composition and microstructure [51].

Recently, doped rare-earth vanadates have been shown to exhibit sufficient conductivity, at least for use as the anode functional layer [32,52,53]. For instance, the electronic conductivity of a composite electrode consisting of 10 vol% $La_{0.7}Sr_{0.3}VO_{3-\delta}$, infiltrated into a porous YSZ8 scaffold, was reported to be greater than 2 S cm^{-1} at 973 K [32]. At 973 K in humidified H_2 the value of P_{max} was 326 mW cm^{-2} and R_P was 0.43 Ω cm^2 if small amounts of Pd and ceria had been added into the anode as the catalysts [32]. For 30 wt% $Ce_{0.7}Sr_{0.3}VO_{3-\delta}$ anode, infiltrated into a porous YSZ8 scaffold and activated additionally with

Pd and ceria, P_{max} was 470 mW cm^{-2} and R_P was 0.3 Ω cm^2 at 973 K in humidified H_2 [52].

As it is demonstrated above, the remarkable disadvantage of ceramic anodes, compared to Ni-cermet anodes, is the lower catalytic activity. However, this can be solved by adding small amounts of a catalyst, for example Ni, Pt, Pd, Rh, Fe and/or ceria, which leads to the significantly lower anode impedances [31,32,46,47,49–52,54–57]. For example, Kim et al [55] showed that the polarization resistance of cells with an $La_{0.8}Sr_{0.2}Cr_{0.5}Mn_{0.5}O_{3-\delta}$-YSZ8-cermet anode decreased from 2.20 Ω cm^2 to 0.14 Ω cm^2 at 973 K in humidified H_2, if 5 wt% CeO_2 and 0.5 wt% Pd catalyst had been infiltrated into the electrode structure. However, several recent papers have indicated that the doped ceria has high catalytic activity [58,59]. If this is true, then the SOFC single cells activated with doped ceria electrolytes and even the doped-ceria based electrodes do not require the addition of other catalysts for the high performance.

4.2. Microstructure of the anode

Microstructure of the electrodes is an important parameter to achieve the maximum electrochemical performance of the SOFC single cells. The electrochemical reactions on SOFC electrodes mostly occur at so-called three-phase boundaries (TPB), which are defined as the lines at which the electrolyte, the electron conducting phase and the gas phase all come together [19]. However, in the mixed ionic and electronic conductors (MIEC) the reaction can also take place at so-called double-phase boundaries (DPB), the region were the MIEC phase, mostly oxide with the perovskite structure, comes together with the gas phase. Therefore, the porosity of the electrode must be sufficiently high to allow the fuel or oxidant transport into the reaction sites and products (H_2O vapor) away from the anode reaction sites. The structure of the solid matrix should guarantee the quick transport of oxide ions and adequate electronic conductivity. In addition it is important to have a high concentration of TPB and/or DPB regions because ions from the electrolyte cannot react in the reaction site, if the gas-phase fuel molecules cannot reach the site, or if the electrons cannot be removed from the site, then the active sites cannot contribute effectively to the performance of the cell [19].

Primary the porosity of the Ni-cermet anode is produced by reducing NiO in the cermet anode to the metallic Ni network by exposure to H_2 at 1073 K or above [33]. The additional porosity of the electrode is usually increased by adding a rational portion of the pore former into the raw material (powder(s)) of the electrode. Sanson et al [60] optimized the microstructure of Ni-YSZ cermet anode, prepared by tape-casting method, by adding four different pore formers (graphite, carbon black, rice starch, potato starch) and a surplus of organic binder in the green tape paste. Based on experimental data analysis, they identified the rice starch and carbon black as the most promising pore formers.

Hu et al [61] reported that the mixture of activated carbon and flour can be used to achieve the desirable porosity of Ni-YSZ-cermet anode. A SOFC single cell based on YSZ thin film electrolyte, SDC-LSM cathode and anode with composite pore formers (activated carbon and flour) had the value of maximum power density 688 W cm^{-2} at 973 K in H_2. Therefore, most commonly the carbon based materials are being used as pore formers, like graphite, flour and rice starch [60–62].

Clemmer and Corbin [63,64] reported that addition of graphite particles as the pore forming agents into Ni-YSZ-cermet anode generated large-scale porosity in the composite samples, the amount of which increased linearly with the graphite content in the green tape.

Zhao and Virkar [65] varied the porosity of the Ni-YSZ composite from 32% to 76% by adding the desirable amount of graphite as a pore former. The value of maximum power density about 0.72 W cm^{-2} was measured at 1073 K for the cell with anode support with 32% porosity, while the value of P_{max} for a cell with anode support with 57% porosity and 76% porosity were approximately 1.55 W cm^{-2} and 1.5 W cm^{-2}, respectively. Also the value of polarization resistance at 1073 K decreased with increasing the porosity (from 0.156 Ω cm^2 to 0.074 Ω cm^2 if porosity increased from 32% to 76%).

Haslam et al [66] also varied the pore former (rice starch) amount in the Ni-YSZ-cermet anode raw material to increase the porosity of the relatively thick supporting anode and improve the gas diffusion inside the anode. It was demonstrated that by increasing the amount of the pore former up to 20 wt% the polarization of the single cell reduced and P_{max} was ~1.2 W cm^{-2} at 1073 K in pure hydrogen. The single cell with the addition of 30 wt% rice starch as the pore former in the raw anode, showed decreased performance relative to the 20 wt% rice starch containing cell, having P_{max} value similar to that for the 10 wt% addition rice starch cell, ~0.9 W cm^{-2} at 1083 K. Haslam et al demonstrated that increasing the porosity of the anode and optimizing the anode microstructure improved the performance of the SOFC single cell. However, the removal of active TPB regions, because of excessive replacement of anode material with pores, decreased the cell performance. Therefore the optimum porosity exists for the SOFC anode, determining the highest power density values.

For characterization of the microstructure of the cermet composite electrode, different methods have been used to determine, for example the porosity, pore sizes, tortuosity, concentration of three-phase boundaries, specific surface area, etc.

Scanning electron microscopy (SEM) is widely used to better understand the porous structure of an electrode (anode and cathode) and to evaluate the pore sizes and composite framework structures. If SEM is combined with the focused ion beam (FIB) method, even 3D structures of the electrodes can be constructed and the porosity, tortuosity, specific surface areas and also length of the three-phase boundaries can be calculated [67]. However, the specific surface

area is most commonly measured by Brunauer-Emmett-Teller (BET) isotherm method. For porosity analysis different methods are being used, like obtaining the weight change of a sample after submersion it into the boiling water, or the mercury intrusion porosimetry method. Pan et al [68] also suggested for calculation of the pore volumes the following formula:

$$PVF = 1 - \frac{\rho}{\rho_0}, \quad (1)$$

where PVF is the pore volume fraction, ρ is the density of a sample, and ρ_0 is the theoretical density of the total compact sample.

4.2.1. Electrode fabrication by applying infiltration method

Synthesis of composite electrodes by infiltration was initially developed to separate the sintering temperature of the electrolyte material from the sintering temperature of the other electrode components [19,69]. However, other advantages became evident, like wider use of electrode materials and easily controlled (not random) microstructure of the electrode so that the sufficient conductivity of anode (or cathode) can be achieved by using perovskite loading below the normal percolation threshold of 30 wt% [70,71]. In general, electrode fabrication by infiltration involves two main steps. Firstly, a porous electrolyte matrix is being developed via dual tape-casting process and the dense electrolyte layer is sintered together with the electrolyte layer containing a pore former to form a porous electrolyte scaffold. In a second step the electron conductive electrode material(s) is infiltrated into the porous electrolyte scaffold [19].

Control of the porosity of the electrolyte scaffold is very important and it must be maintained after applying firing temperatures sufficient to form the dense electrolyte layer. The structure of the scaffold pore walls is of critical importance since one needs to maintain ion-conducting pathways. Also the porosity of the electrolyte scaffold materials needs to be much higher for infiltrated electrodes due to the requirement for maintaining porosity for gas-phase diffusion after the addition of significant amount of the perovskite electrocatalyst [70].

Porosity and the pore structure of the porous electrolyte scaffold can be controlled by using variable pore forming agents, and also by varying the amount of the pore forming agents. Corbin and Prasad [72] reported that porosity characteristics of sintered YSZ tapes, prepared by tape-casting, were directly controlled by the amount, size (19, 82 or 210 μm) and distribution of the pore-forming agents (starch, graphite or polyethylene, respectively) added to the green tape, as well as adjustments made to the tape formation. It was found that the most effective pore former was graphite with an average particle size of

80 μm, and completely open porous structures with bulk porosities ranging from 20% to 80% were created without significantly altering sintering shrinkage [72]. It has been reported in other studies [73,74] that using of the spherical polymethyl methacrylate (PMMA) as a pore former leads to the spherical cavities (~30 μm in size) in the YSZ ceramic, while the dependence between the cavity parameters and graphite pore former shape was less clear. However, the size of the pores was certainly comparable to the size of the graphite particles.

Küngas et al [73] reported that modifying the microstructure of the porous YSZ bulk scaffold through an HF-treatment before infiltration of the LSF cathode increased the electrode performance noticeably. After HF-treatment the sheet- and pillar-like structures of YSZ scaffold with the specific surface area of 2.1 m g^{-1} were seen instead of "sponge-like" structure with the specific surface area of 0.48 m g^{-1} for untreated with HF etching. Low nonohmic losses, calculated from impedance spectra, were 0.07 Ω cm^2 and 0.13 Ω cm^2 at 973 K for HF-treated and non-treated cells, respectively [73].

However, it was found that wet-etching of cerium oxide with HF is more complicated than that of zirconium oxide. This is because of the poor solubility of Ce^{4+} ion in water and in other polar solvents compared to Zr^{4+} ion. Even if Ce^{4+} ion is transferred into the solution it has the tendency to precipitate in a form of $CeO_{2-\delta}$ [75]. However, based on Rupp et al study [76], the etching rate of GDC (with crystal structure) with 10% HF in H_2O solution was 0.002±0.001 μm min^{-1} and the increase in the specific surface area was reported with the rate of 0.62±0.03 area% min^{-1}. In other studies, 10% HF in H_2O solution has been used to increase the roughness of the sintered gadolinium doped cerium oxide pellet [77] and to etch the gadolinium doped cerium oxide thin films [78].

4.3. Electrochemical reactions in SOFC electrodes

The oxygen reduction takes place on the cathode:

$$O_2 + 4e^- \rightarrow 2O^{2-} \tag{2}$$

and hydrogen/hydrocarbon oxidation on the anode:

$$C_nH_{2n+2} + (3n + 1)O^{2-} \rightarrow nCO_2 + (n + 1)H_2O + (6n + 2)e^- \tag{3}$$

Therefore, the overall electrochemical reaction at the SOFC is:

$$H_2 + ½O_2 \rightarrow H_2O. \tag{4}$$

All of these electrochemical reactions take place at the three-phase boundary regions and simultaneously at the double-phase boundary regions if mixed ionic and electronic conductors are being used as the electrode materials.

The maximum theoretical cell potential, E_N, i.e., Nernts potential generated by the SOFC is related to the Gibbs free energy difference across the electrolyte membrane accordingly to the well-known Nernst equation:

$$E = \frac{RT}{4F} \ln \frac{P_{O_2}(cathode)}{P_{O_2}(anode)}, \quad (5)$$

where R is the gas constant, T the temperature, F the Faraday constant and P_{O2} the partial pressure of oxygen at the electrode and 4 is the number of electrons participating in the electrochemical reaction (if H_2 is being used as a fuel) [5]. For humidified hydrogen fuel the corresponding Nernst potential values at 773 K, 782 K and 873 K are 1.154 V, 1.146 V and 1.138 V, respectively. However, the voltage produced by the working SOFC is somewhat less than the theoretical Nernts value [8,56,79–81] because of the ohmic losses associated with the transport of the ions through the electrolyte (jR_{tot} is so called ohmic loss where j is the current density applied and R_{tot} is the total resistance), finite rates of the electrode reactions (so called polarization losses) as well as by the gas and electron transport in the electrodes [33]. The electrolyte losses can be reduced by using a very thin electrolyte layer to increase the ionic conductivity of the electrolyte. The polarization losses associated with the rate of electrochemical reaction can be minimized by improving the catalytic activity and optimization of the microstructure.

The oxygen reduction on the cathode is usually the rate limiting step obtaining mainly SOFC performance and therefore has been thoroughly investigated by various studies [11,14–16]. The mechanism of oxygen reduction inside a MIEC cathode is thought to proceed along two possible pathways. Near the cathode|electrolyte interface, the reaction is considered to occur mainly in the TPB region according to the following mechanism [82,83]:

$$\text{Dissociative adsorption: } O_2(g) \Leftrightarrow 2\,O_{ads} \quad (6)$$

$$\text{Surface diffusion: } O_{ads} \Leftrightarrow O_{TPB} \quad (7)$$

$$\text{Charge transfer: } O_{TPB} + 2e^- \Leftrightarrow O_{TPB}^- + e^- \Leftrightarrow O_{TPB}^{2-} \quad (8)$$

$$\text{Oxygen incorporation: } O_{TPB}^{2-} + V_O^{\bullet\bullet} \Leftrightarrow O_O^{\times} \quad (9)$$

However, in regions further from the TPB, an alternative mechanism has been proposed that involves the diffusion of O^{2-} into the MIEC bulk [82]:

$$\text{Dissociative adsorption: } O_2(g) \Leftrightarrow 2\,O_{ads} \quad (10)$$

$$\text{Charge transfer: } O_{ads} + 2\,e^- \Leftrightarrow O_{ads}^- + e^- \Leftrightarrow O_{ads}^{2-} \quad (11)$$

$$\text{Bulk diffusion: } O_{ads}^{2-} \Leftrightarrow O_{electrolyte}^{2-} \quad (12)$$

$$\text{Oxygen incorporation: } O_{electrolyte}^{2-} + V_O^{\bullet\bullet} \Leftrightarrow O_O^{\times} \quad (13)$$

The rate-limiting step is usually determined through temperature and oxygen partial pressure variation experiments. Lu et al [35] determined a charge transfer as the rate-determining step for the cathode reaction at the LSCF cathode in flowing oxygen. However, in flowing air the diffusion of molecular oxygen as a limiting step has been established using electrochemical impedance spectroscopy method (i.e. as the scale semicircle at Nyquist plot at very low frequencies) A mathematical model developed for LSF and LSM cathodes infiltrated into YSZ scaffold suggests that two rate-limiting steps occur: (*i*) oxygen ion diffusion through the perovskite film or (*ii*) dissociative reactive adsorption of O_2 at the perovskite surface (reaction between the gase-phase O_2 molecules adsorbed and oxygen vacancies in surface layer) [84].
The complicated mechanism for the hydrogen oxidation on Ni-YSZ anodes takes place mainly on electrochemically active TPB sites consisting of the following steps (while hydrogen is being used as a fuel) [85]:

$$\text{Dissociative adsorption: } H_2(g) \Leftrightarrow 2\,H_{ads} \tag{14}$$

$$\text{Surface diffusion: } H_{ads} \Leftrightarrow H_{TPB} \tag{15}$$

$$\text{Hydroxyl anion formation: } H_{TPB} + O_O^{\times} - e^- \Leftrightarrow OH_{TPB}^- + V_O^{\bullet\bullet} \tag{16}$$

$$\text{Water formation: } H_{TPB} + OH_{TPB}^- - e^- \Leftrightarrow H_2O_{TPB} \tag{17}$$

$$\text{Water desorption: } H_2O_{TPB} \Leftrightarrow H_2O(g) \tag{18}$$

Probably the same mechanism can be used for describing the hydrogen oxidation on the ceramic anode at the MIEC oxide|electrolyte interface. However, an alternative mechanism may appear at the bulk MIEC:

$$\text{Dissociative adsorption: } H_2(g) \Leftrightarrow 2\,H_{ads} \tag{19}$$

$$\text{Hydroxyl formation: } H_{ads} + O_O^{\times} - e^- \Leftrightarrow OH_{ads}^- + V_O^{\bullet\bullet} \tag{20}$$

$$\text{Water formation: } H_{ads} + OH_{ads}^- - e^- \Leftrightarrow H_2O_{ads} \tag{21}$$

$$\text{Water desorption: } H_2O_{ads} \Leftrightarrow H_2O(g) \tag{22}$$

At low current densities the rate limiting steps on anode are probably the bulk gas and surface diffusions and the demand for reactive TPB sites is low. However, at higher fuel utilization rates, the demand for reactive site increases and, consequently, many of the reactive sites are occupied by either the adsorbed hydrogen atoms, H_{ads}, waiting for oxidation by an O^{2-}, or by OH_{ads}^-, as well as even by slowly desorbing H_2O_{TPB} species. Thus the new reactants cannot reach to the TPBs directly from the gas phase and, thus, the surface and bulk diffusion operates probably in series. However, it should be noted that the slower surface diffusion mechanism controls the supply of reactants to the TPB [85].

4.4. Methods for electrochemical characterization of SOFCs properties

The main techniques for SOFC electrochemical characterization and determination of the cell potential losses in SOFC are: (*i*) cyclic voltammetry, and (*ii*) electrochemical impedance spectroscopy.

4.4.1. Cyclic voltammetry

Cyclic voltammetry (CV) is an electrochemical method, where the potential of the system is changed linearly with the time, from the initial potential to the final potential and then swept back to the initial potential, and the current density of the system is being recorded. Figure 1a illustrates the current-potential (*j–E*) plot for an operating SOFC [5,3]. Under ideal conditions the constant potential would be expected (straight line parallel to the current axis if no polarization, ohmic (*jR* drop) and mass-transfer losses occur). For real systems there are three main regions, where the three different processes, i.e. the potential losses of the single cell, can be separated. At the low current densities the major contribution of the single cell potential losses is generated by the activation polarization (indicated by the sharp drop in cell potential with increasing current). With the medium cell current region the ohmic polarization losses (indicated by the linearity) prevail. Finally, at very high current densities, the single cell behavior, i.e. the resistance, is controlled by the mass transport limitations (expressed as the rapid decrease in cell voltage) [5,24].

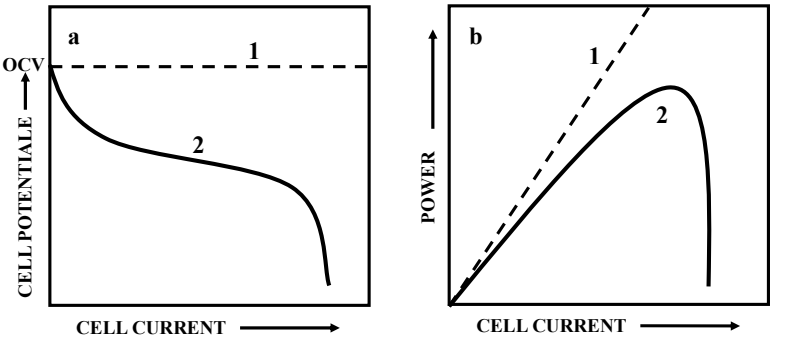

Figure 1. a) Typical cell potential vs. cell current relationship for an ideal (1) and real operating fuel cell (2), and b) typical power vs. cell current plot for a hypothetical ideal (1) and real (2) fuel cell. [5]

From current density vs. cell potential (*j–E*) dependence the power density, *P*, of the SOFC can be calculated:

$$P = Ej, \tag{23}$$

where j is the current density and E is the responding cell potential of the SOFC. For ideal SOFC the linear dependence of P on j can be predicted, shown in Fig. 1b [5]. For real working SOFC it is difficult to obtain a general expression for maximum power density value when all forms of the cell potential losses, including activation and mass-transfer over potentials and ohmic polarizations, are present. However, it can be approximately done in the region, where the cell potential varies linearly with the current [5].

4.4.2. Electrochemical impedance spectroscopy

Electrochemical impedance spectroscopy (EIS) is a very powerful technique for the electrical characterization of electrochemical systems. The strength of EIS method lies in the fact that by small-signal perturbation it reveals both the relaxation times and relaxation amplitudes of the various processes present in a dynamic system over a wide range of frequencies [3].

In an EIS experiment, the impedance of an electrochemical system is determined by applying a low amplitude alternating potential $U(t)$ to a steady-state potential U_0 and measuring the phase shift and the amplitude of the resulting current. The perturbation signal has the form

$$U(t) = U_0 \cos(\omega t), \tag{24}$$

where $\omega = 2\pi f$ is the angular frequency, f the frequency of the alternating potential and t is the time. If the applied potential is sinusoidal, then the subsequent current $I(t)$ will also be sinusoidal, and is given as

$$I(t) = I_0 \cos(\omega t - \varphi), \tag{25}$$

where I_0 denotes current amplitude and φ stands for the phase shift between potential and current. The relationship between the applied potential and the current flow is known as impedance. The impedance, $Z(t)$, has a magnitude

$$Z(t) = \frac{U(t)}{I(t)} = \frac{U_0 \cos(\omega t)}{I_0 \cos(\omega t - \varphi)} \tag{26}$$

and a phase φ and is thus a vector quantity [86,87]. By measuring the phase shift and the amplitude of the resulting current at different frequencies, it is a common practice to express the impedance vector by the vector sum of the real (Z') and imaginary (Z'') components along the axes, that is, by a complex number

$$Z(\omega) = Z'(\omega) + iZ''(\omega), \tag{27}$$

where $i = \sqrt{-1}$.

Dependence of real vs. imaginary components is described by so-called Nyquist plot (Figure 2). Point, where the spectrum intersects with the real-axis corresponds to the high frequency series resistance so-called ohmic resistance, R_Ω. Usually this resistance is directly related to the dense electrolyte and its thickness. Line segment underneath the semicircle corresponds to the difference between the low frequency series resistance and high frequency resistance usually known as polarization resistance, R_P, which is the sum of all resistances of the anode and cathode electrochemical processes, including slow transfer steps [19].

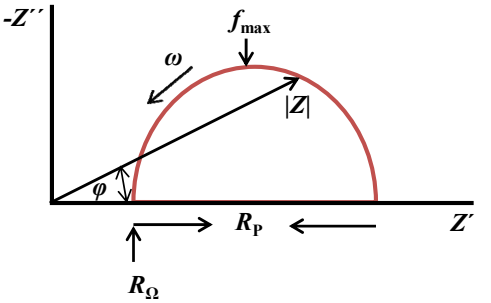

Figure 2. Nyquist plot.

$R_{tot}(\omega\rightarrow\infty)$ is a very complex parameter and in addition to the electrolyte resistance it contains resistance of current collector|electrolyte interface as well as the electrolyte|electrode (electrolyte|anode and electrolyte|cathode) interfaces, i.e. consists of all polarization components, discussed above.

Under reducing conditions a weak electronic contribution to the electrochemical impedance, if ceria based mixed conductor is being used as an electrolyte, can occur. Liu et al and Haile et al [79,88–91] have suggested simplified equation to evaluate the weak electronic contribution for the ceria based electrolyte as:

$$R_P = \frac{R_{tot}-R_\Omega}{\frac{OCV}{E_N}\left[1-\frac{R_\Omega}{R_{tot}}\left(1-\frac{OCV}{E_N}\right)\right]} \quad (28)$$

where OCV is the open circuit voltage, E_N is the Nernst potential of the cell, R_Ω is the intercept of the impedance with the real axis at high frequencies ($R_{tot}(\omega\rightarrow\infty)$) and R_{tot} is the intercept at the low frequencies (total resistance of the impedance) ($R_{tot}(\omega\rightarrow0)$).

4.4.3. Alternative analysis of impedance spectra

The total resistance of the SOFC single cell measured by EIS contains contribution from many processes. In order to improve the performance of a

single cell it is important to determine the contributions from specific components or processes influencing the total impedance. However, separation of contributions of the anodic and the cathodic processes taking place in the SOFC single cell is complicated because all the processes are somewhat influenced by the temperature and change of the cell potential influencing the rates of the cathodic as well as anodic charge transfer processes.

Barford et al [92] and Jensen et al [93] have developed the method based on the analysis of differences in impedance spectra (ADIS) in order to better estimate and separate the processes occurring in a SOFC single cell. It is an empirical method to estimate the changes in impedance spectra caused by one variable that had been changed during the measurements at the condition of the fixed other parameters.

Barford et al [92] constructed the ADIS spectrum in order to convolute the cell response into anodic and cathodic contributions. Most likely anodic processes correspond to the frequency range which is affected by the change of hydrogen partial pressure in the fuel compartment under constant oxidant flow and cell potential conditions. Difference between the derivatives of the spectrums obtained at different hydrogen partial pressures can be calculated accordingly:

$$\Delta\partial Z_{anodic} = \frac{\partial|Z_{p1(H_2)}|}{\partial \log f} - \frac{\partial|Z_{p2(H_2)}|}{\partial \log f} \tag{29}$$

By plotting $\Delta\partial Z_{anodic}$ vs. frequency dependencies the corresponding frequency range where the anodic processes occur can be found [92,94]. Based on the literature data [92,95] up to three arcs have been reported for the impedance spectra measured for Ni-YSZ cermet anode based cell. First semicircle, at a high-frequency range, corresponds most likely to the charge transfer process between YSZ and Ni network as well as to diffusion of charged species to the TPB [93,96]. The second arc can be observed in a so-called mid-frequency region ($10<f<100$ Hz) due to the slow gas diffusion [97] and the third arc in a low-frequency range ($f<10$ Hz) is related to the gas conversion [98].

Similarly to the anodic processes, the cathodic processes can be analyzed by changing the partial pressure of oxygen in the cathode compartment under constant fuel composition and cell potential applied [93,94]. Difference between the derivatives of the spectrums obtained at different oxygen partial pressures can be calculated accordingly:

$$\Delta\partial Z_{cathodic} = \frac{\partial|Z_{p1(O_2)}|}{\partial \log f} - \frac{\partial|Z_{p2(O_2)}|}{\partial \log f} \tag{30}$$

For the cathodes up to five limiting steps has been reported [92], however only two primary arcs for LSM-YSZ can be described in the impedance spectrum clearly. The high-frequency arc has been suggested to be associated with

transport-transfer of oxygen ions at the LSM|YSZ interface and trough YSZ. The low-frequency arc has been ascribed to the disoactive adsorption of O_2 followed by the electrochemical reduction and transfer of oxygen species at the TPB [92]. However, it has also been shown by Bidrown et al [84] that the characteristic frequencies cannot be used to distinguish where diffusion or adsorption is a rate-limiting step, at least for LSM and LSF cathodes, infiltrated into YSZ scaffold.

ADIS method can also be used to evaluate the differences in the impedance spectra at other changing cell parameters beside hydrogen and oxygen partial pressure. For example, cathode performance can be evaluated at various cell potentials, E_{fix}, under constant hydrogen and oxygen partial pressures [94,99]:

$$\Delta\partial Z_{potential} = \frac{\partial\left(Z_{E_{OCV}}\right)}{\partial \log f} - \frac{\partial\left(Z_{E_{fix}}\right)}{\partial \log f} \tag{31}$$

It has to be remembered, that the change of partial pressure of hydrogen in fuel gas or oxygen in oxidant, carried out at constant cell potential conditions, incur the potential change of both electrodes and therefore, additionally to the impedance change of anode process also small change in impedance of the cathode process is possible and vice versa.

4.4.4. Fitting of impedance data

In order to investigate the EIS data in more detail the characteristics impedance (i.e. resistance and capacitance) values of the impedance arcs can be calculated using the equivalent circuit (EC) modeling method. Figure 3 shows some examples of the equivalent circuits that have been used for SOFCs. These EC are based on physical models of interface discussed in Ref. 93–95.

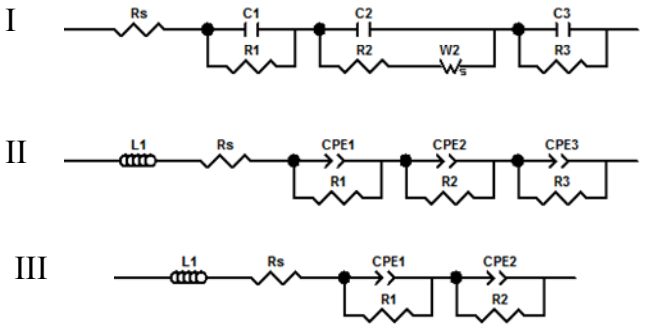

Figure 3. Equivalent circuits used for the fitting of experimental impedance spectra.

In these ECs L characterizes the high-frequency inductance, R_s is the high-frequency series resistance of a system, C is capacitance, W is a short circuit Warburg impedance, CPE is constant phase element, and R is characteristic resistance of the semicircle. All these three ECs are quite common for modeling

of the processes in Ni-cermet anode SOFC [35] enable define and separate some basic characteristics of processes with relatively similar time constants. The detailed EC depends strongly on the anode, cathode and electrolyte characteristics including the chemical composition and microstructure of the electrodes as well as thickness of the electrolyte.

5. EXPERIMENTAL

5.1. Single cell preparation

In this work mainly SOFCs with three different configurations were prepared and tested: (*i*) electrolyte supported Ni-$Ce_{0.9}Gd_{0.1}O_{2-\delta}$|$Ce_{0.9}Gd_{0.1}O_{2-\delta}$|$La_{0.6}Sr_{0.4}CoO_{3-\delta}$ single cell (noted as ES Ni-GDC10|GDC10|LSC40), (*ii*) anode supported Ni-$Ce_{0.9}Gd_{0.1}O_{2-\delta}$|$Zr_{0.94}Sc_{0.06}O_{2-\delta}$-$Ce_{0.9}Gd_{0.1}O_{2-\delta}$|$La_{0.6}Sr_{0.4}CoO_{3-\delta}$ single cell (noted as AS Ni-GDC10|ScSZ6-GDC10|LSC40), and (*iii*) electrolyte supported $La_{0.7}Sr_{0.3}VO_{3-\delta}$-$Ce_{0.85}Sm_{0.15}O_{2-\delta}$|$Ce_{0.85}Sm_{0.15}O_{2-\delta}$|$Ce_{0.85}Sm_{0.15}O_{2-\delta}$-$La_{0.8}Sr_{0.2}CoO_{3-\delta}$ single cell (noted as ES LSV30-SDC15|SDC15|SDC15-LSC20).

5.1.1 Preparation of the electrolyte supported Ni-GDC10|GDC10|LSC40

The supportive electrolyte pellet was prepared by dry-pressing of the commercial GDC10 powder (99.9%, NexTech, S_{BET}=19.9 m^2g^{-1}) at 90 MPa, followed by a 15 h sintering cycle at 1773±2 K in a high-temperature furnace (Carbolite HTF-1700). The resulting pellets were approximately 19.9±0.1 mm in diameter and 720±10 μm in thickness.

The anode was built up in two layers, so-called functional and diffusion layers. The functional layer was prepared from the mixture of commercial NiO and GDC10 with S_{BET}=70.8 m^2g^{-1}. More porous anode diffusion layer was prepared from commercial NiO-GDC (S_{BET}=6.5 m^2g^{-1}) with addition of 1 wt% of carbonaceous pore former (carbon black, acetylene 100%, compressed, purity 99.9%, Alfa Aesar) in the raw anode paste. Both anode layers were screen printed onto the sintered electrolyte pellet through 200 mesh screen and sintered at 1623±2 K for 5 h.

The cathode powder was prepared by the nitrate solution thermal combustion method using $La(NO_3)_3 \cdot 6H_2O$, $Sr(NO_3)_2 \cdot 6H_2O$ (both 99.9%, Aldrich) and $Co(NO_3)_2 \cdot 6H_2O$ (98%, Riedel de Haën) as precursors for synthesis of $La_{0.6}Sr_{0.4}CoO_{3-\delta}$ (LSC40) cathode powder, and glycine (99.9%, Sigma Aldrich) was used as a reducing agent. $La(NO_3)_3 \cdot 6H_2O$, $Co(NO_3)_2 \cdot 6H_2O$, and $Sr(NO_3)_2$ where dissolved in $MilliQ^+$ water and thereafter the calculated amount of glycine, dissolved in $MilliQ^+$ water, was slowly added under moderate stirring to receive a real solution. The solution was heated on a hot plate to form a viscous solution and thereafter added dropwise into a Pt-beaker that was preheated to the temperature range from 575 to 675 K. The solvent was quickly evaporated and the corresponding reagents reacted autothermally to form the fine size structural complex oxide LSC40 nanopowder. To get better phase purity and the additional calcination and partial sintering of the nanopowder materials was carried out at T≥1373K during 8 h. The cathode paste was prepared from LSC40 powder and screen printed, similarly to the anode layers,

onto the other side of the electrolyte pellet, and fired at 1423±2 K for 5 h. [14–16,94].

Both anode and cathode had the geometrical flat cross section surface area of 1.65 cm^2. The platinum paste (MaTeck) was screen printed through the 450 mesh screen onto the both electrodes in order to ensure good electrical contacts of anode and cathode with current collectors.

5.1.2. Preparation of the anode supported Ni-GDC10|ScSZ6-GDC10|LSC40

The supportive raw anode pellet was prepared by dry-pressing the commercial NiO-GDC10 powder (Fuel Cell Materials, 60% NiO and 40% GDC10 by weight, S_{BET} = 6.57 m^2g^{-1}) at 8.6 kN cm^{-2}, where graphite powders (with different amount and graphite particle size distribution (Figure 4)) were added as pore formers, and followed by 3 h sintering at 1623±2 K in a high-temperature furnace (Carbolite HTF-1700). All together 13 supportive anodes with different microstructures (Table 1) were prepared with the approximate diameter of 21±1 mm and thickness of 700±50 μm.

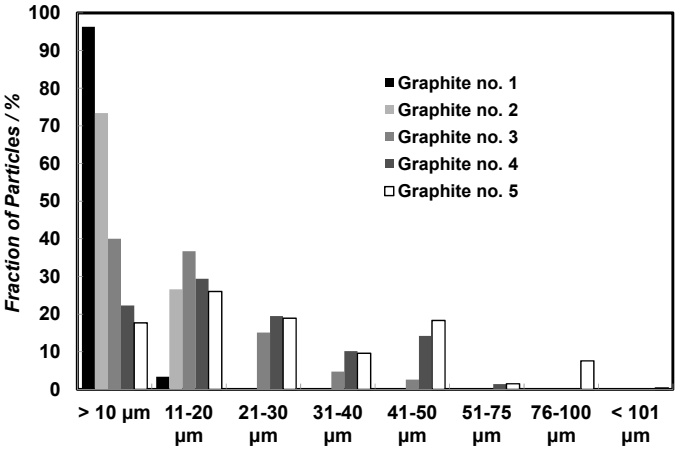

Figure 4. Particle size distribution for five different graphite powders used as pore formers.

Table 1. Wt% of pore formers and bulk vol% of powders (based on Scott volumetric density values) used in the raw supporting anode material, pore volume fraction *PVF* (calculated according to Equation 1) before reducing, and total pore volume, P_{tot}, measured after reducing of an anode.

	Pore former	wt%	vol%	*PVF*	P_{tot}
Ni-cell 0	No pore former	0	0	–	–
Ni-cell 1	Graphite no. 1 (S_{BET}=20.0 m^2 g^{-1})	1	3.2	9.8	34.2
Ni-cell 2	Graphite no. 1	1.5	4.8	10.7	–
Ni-cell 3	Graphite no. 1	2	6.3	11.1	–
Ni-cell 4	Graphite no. 1	2.5	7.8	11.5	–
Ni-cell 5	Graphite no. 1	3	9.2	12.3	39.9
Ni-cell 6	Graphite no. 1	3.5	10.6	12.7	–
Ni-cell 7	Graphite no. 1	4	12.0	13.1	40.8
Ni-cell 8	Graphite no. 1	3	9.2	12.3	–
Ni-cell 9	Graphite no. 2 (S_{BET}=16.0 m^2 g^{-1})	3	7.3	10.8	–
Ni-cell 10	Graphite no. 3 (S_{BET}=12.0 m^2 g^{-1})	3	4.8	10.7	–
Ni-cell 11	Graphite no. 4 (S_{BET}=9.0 m^2 g^{-1})	3	3.6	10.1	–
Ni-cell 12	Graphite no. 5 (S_{BET}=6.5 m^2 g^{-1})	3	2.9	10.4	39.2

The anode active layer was screen printed onto the sintered supportive anode pellet by applying the commercial NiO-GDC10 ink (Fuel Cell Materials) through 200 mesh screen and fired at 1623±2 K for 3 h. The electrolyte membrane layers were screen printed onto the anode active layer using the commercial scandia stabilized zirconia (ScSZ6 (ESL)) and gadolinia doped ceria (GDC10 (ESL)) electrolyte pastes. Two layers of ScSZ6 were printed as the electrolyte and two layers of GDC10 as the chemical barrier layers. Each electrolyte layer was sintered separately at 1623±2 K for 3 h. Figure 5a shows the cross-sectional SEM image of the anode supported single cell (Ni-cell 1). The prepared electrolyte layers are both approximately 15 μm thick and deposited ScSZ6 layer is nonporous. Finally, the LSC40 cathode was screen printed onto the GDC10 membrane layer using the same procedure as for electrolyte supported cell (discussed above). Like for the electrolyte supported Ni-cermet anode containing single cell, the cathode geometrical surface area was 1.65 cm^2.

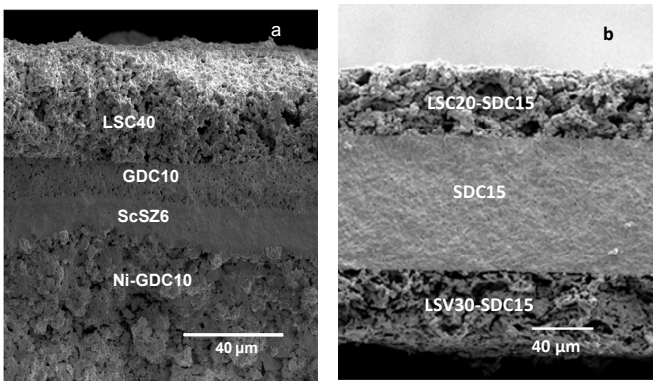

Figure 5. SEM image of cross-section of a) AS Ni-cermet anode containing single cell (Ni-cell 1) and b) ES LSV30-cermet anode containing single cell (LSV-cell no 1).

5.1.3. Preparation of the electrolyte supported LSV30-SDC15|SDC15|SDC15-LSC20

Infiltration method was used for preparation of the electrolyte supported ceramic anode containing cells. The SDC15 wafers (dense electrolyte disc sandwiched between two porous SDC15 scaffolds) were built up from SDC15 tapes made by tape casting. The wafers were fabricated by laminating the four green tapes (porous-dense-dense-porous) followed by sintered at 1773±2 K for 4 h. The scheme of SOFC preparation by infiltration method is shown in Figure 6 and the cross-section of the single cell in Figure 5b.

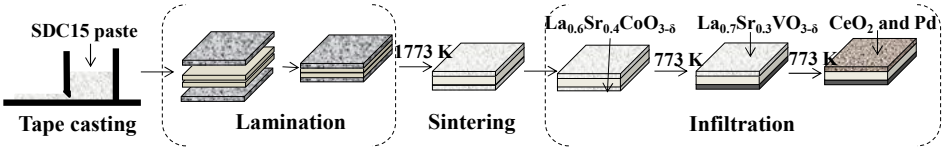

Figure 6. Scheme of SOFC preparation by infiltration method.

The tapes used in this work were cast from a slurry based on organic solvents. For the dense electrolyte layer, the tape-casting slurry was prepared by adding the $Ce_{0.85}Sm_{0.15}O_{2\delta}$ powder (Fuel Cell Materials) into a mixture of the solvent (ethanol and xylenes in a weight ratio 17:10) and a dispersant (Menhaden fish oil). After ball-milling of this mixture for 24 h the binder (polyvinylbutyral B-98) was added, followed by the ball milling step for another 24 h before adding the plasticizers (polyethylene glycol 400 MW; benzyl butyl phthalate). The slurry was subsequently ball-milled for an additional 24 h. The green tapes were cast onto the Mylar tape.

The green tapes used for the porous electrolyte layers ware prepared in a similar manner except that a different ethanol-to-xylene ratio (2.5:10) was used

to accommodate the addition of the pore formers (graphite no. 6 (synthetic graphite, 300 mesh from Alfa Aesar), graphite no. 3, graphite no. 5 and graphite no. 7 (particle size was less or equal 20 μm from Fluke)). Some porous SDC15 electrode scaffolds microstructure was additionally changed by wet etching of the SDC15 framework with hydrofluoric acid. The HF treatment was carried out simply by infiltrating the porous scaffold with concentrated HF solution (ACS reagent grade, MP Biomedicals) at room temperature. The solution was then left in the scaffold for 1 h and removed by washing the porous SDC15 scaffold several times with distilled water. Only one side of the porous SDC15 scaffold was treated with aqueous HF solution, where the LSV30 anode was introduced by infiltration step.

Catalytically active ceramic $La_{0.7}Sr_{0.3}VO_{3-\delta}$ (LSV30) anode (with perovskite structure) and $La_{0.8}Sr_{0.2}CoO_{3-\delta}$ (LSC20) cathode were fabricated by infiltrating the porous SDC15 scaffolds with aqueous solutions. The anode solution consisted of $La(NO_3)_3 \cdot 6H_2O$ (99.9%, Alfa Aesar), $Sr(NO_3)_2$ (99.9%, Alfa Aesar) and NH_4VO_3 (99.9%, Alfa Aesar) in a molar ratio of La:Sr:V=0.7:0.3:1, and the cathode solution consisted of $La(NO_3)_3 \cdot 6H_2O$ (99.9%, Alfa Aesar), $Sr(NO_3)_2$ (99%, Alfa Aesar), and $Co(NO_3)_2 \cdot 6H_2O$ (99%, Aldrich,) in a molar ratio of La:Sr:Co=0.8:0.2:1. Citric acid in a molar 1:1 ratio (metal cations) was used as a complexing agent in order to assist the formation of the perovskite phase at lower synthesis temperatures. Infiltration steps were followed by a 0.5±0.08 h heat treatment at 723±5 K to decompose the nitrates used. This procedure was repeated until a desired loading of LSV30 and LSC20 was achieved, and followed by sintering at 973±2 K. It should be noted that the cathode composite was prepared before the anode in all cases under study. As a final step in cell preparation, 5 wt% CeO_2 and/or 1 wt% Pd were deposited onto the LSV30-SDC15 composite (in order to increase the catalytic activity) by infiltration of 1 M $Ce(NO_3)_3$ (99.9%, Alfa Aesar) and 0.45 M tetraammine palladium(II) nitrate (99.9%, Alfa Aesar) solutions, followed by calcination at 723±0.08 K for 0.5±0.08 h. The exact composition of the anode and the cathode for the eight ceramic SOFC single cells tested is presented in Table 2.

Table 2. ES LSV30-cermet anode containing single cells prepared via infiltration method

Single cell no.	Porous SDC15 scaffold porosity	SDC|LSC cathode	SDC|LSV anode	Anode catalysts
LSV-cell 1	59±1% (water submersion) (graphite no. 6)	25±0.5% LSC20	31±0.5% LSV30	none
LSV-cell 2	59±1% (water submersion) (graphite no. 6)	25±0.5% LSC20	31±0.5% LSV30	5±0.5% CeO_2
LSV-cell 3	59±1% (water submersion) (graphite no. 6)	25±0.5% LSC20	31±0.5% LSV30	1±0.5% Pd
LSV-cell 4	59±1% (water submersion) (graphite no. 6)	25±0.5% LSC20	31±0.5% LSV30	5% ±0.5 CeO_2, 1%±0.5 Pd
LSV-cell 5	59±1% (water submersion) (graphite no. 6)	25±0.5% LSC20	31±0.5% LSV30	5% ±0.5 CeO_2, 1%±0.5 Pd
LSV-cell 6	75% (FIB-SEM data) (graphite no. 3)	35±0.5% LSC20	20±0.5% LSV30	5% ±0.5 CeO_2, 1%±0.5 Pd
LSV-cell 7	60% (FIB-SEM data) (graphite no. 5)	35±0.5% LSC20	20±0.5% LSV30	5% ±0.5 CeO_2, 1%±0.5 Pd
LSV-cell 8	57% (FIB-SEM data) (graphite no. 7)	35±0.5% LSC20	20±0.5% LSV30	5% ±0.5 CeO_2, 1±0.5% Pd

5.2. Experimental measurement setups and physical characterization of the electrode materials

All SOFC single cells prepared were characterized electrochemically using impedance spectroscopy and cyclic voltammetry carried out by using Solatron 1260 frequency response analyzer in conjunction with Solatron 1287A potentiostat/galvanostat electrochemical interface (accuracy of the instrument: 0.1–1%, depending on the frequency range and resistance value [100]) or Gamry Instruments potentiostat Interface 1000. Electrical contact was created using Pt-mesh and Pt-wires (Ni-cermet cells) or by Ag paste and Ag-wires (LSV30-cremet anode containing single cells).

Three different experimental setups (Figure 7) were used taking into account the physical properties of the cells and the SOFC single cell preparation technology improvements made. The electrolyte supported Ni-cermet anode containing single cell was fixed between two alumina tubes using gold ring (NexTech Materials) on the anode side and the fibre-free high-temperature sealing welt (Microtherm) on the cathode side as sealing material between the tube the single cell (Figure 7a). The system was placed horizontally inside a tube furnace (Carbolite MTF12/38/400). The anode supported Ni-cermet containing single cell was fixed in a vertical ProboStat measurement cell (Norvegian Electrochemic test ring) (Figure 7b) and placed also inside a tube

furnace (Carbolite). A gold ring and gold ink (Fuel Cell Materials) were used to seal the anode compartment from the cathode compartment. The electrolyte supported LSV30-cermet anode containing single cell was simply attached to an alumina tube using a ceramic adhesive (Ceramobond 552, Aremco) to seal the anode compartment while the cathode was opened to the ambient air (Figure7c).

For all three experimental setups, fuel was fed through the alumina tube onto the anode surface with the flow rates 100 ml min^{-1} (ES Ni-cermet anode containing single cells and ES LSV30-cermet anode containing single cells) or 50 ml min^{-1} (AS Ni-cermet anode single cells or ES LSV30-cermet anode containing single cells). As a fuel, the humidified H_2 and the mixture of H_2 and Ar was used. For ES LSV30-cermet containing single cells in addition to H_2, humidified CH_4 was used in some experiments. Air or the mixture of O_2 and N_2 was used as oxidant. Only in case of the ES LSV30-cermet anode containing single cells the cathode was directly opened to the ambient air (Figure 7c). The flow rates of the gases used were controlled by digital mass flow controllers (Alborg or Bronkhost (accuracy 0.5% [101]) or by manual gas flow meters from Brooks Instrument Division (self-calibrated)).

The electrochemical measurements were carried out at working temperatures from 773±2 K to 973±2 K varying the potential of the single cells, the partial pressure of H_2 in the fuel and the partial pressure of O_2 in the oxidant (only for Ni-cermet anode containing single cells).

The microstructures of the electrodes were analyzed using SEM or FIB-SEM methods. The specific surface area values were measured using BET method and calculated from isotherms. The formation of desired $La_{1-x}Sr_xVO_{3-\delta}$ form was verified by X-ray diffraction method.

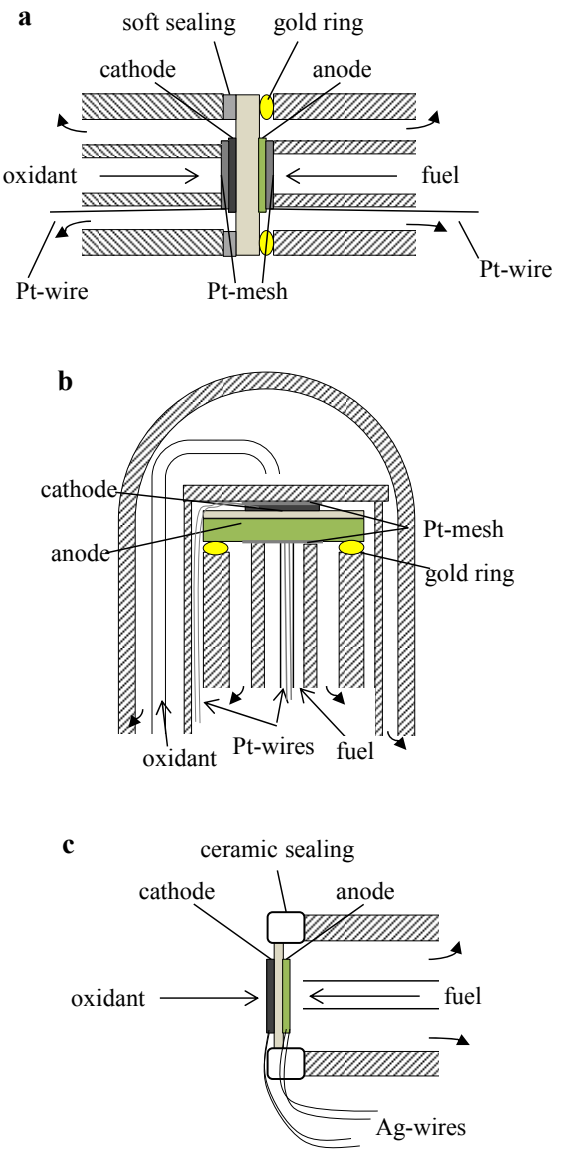

Figure 7. Experimental setup used for a) ES Ni-GDC10|GDC10|LSC40 single cell, b) AS Ni-GDC10|ScSZ6-GDC10|LSC40 single cell, and c) ES LSV30-SDC15|SDC15|SDC15-LSC20 single cell.

6. RESULT AND DISCUSSION

6.1. Electrochemical impedance spectroscopy [Papers I–IV]

Electrochemical impedance spectroscopy measurements were carried out with in the frequency range from 0.1 Hz to 100 kHz and with an AC perturbation of 5 mA at various cell temperatures, potentials and hydrogen and/or oxygen partial pressures. In addition, nonlinear least square fitting of calculated impedance spectra to experimental ones is used. Corresponding equivalent circuits are shown in Figure 3: I for ES Ni-GDC10|GDC10|LSC40, II for AS Ni-GDC10|ScSZ6-GDC10|LSC40, and III for ES LSV30-SDC15|SDC15|SDC15-LSC20 single cell.

Figure 8 shows Nyquist plots for SOFC single cells with different cell design, configuration and preparation methods. Electrolyte supported Ni-cermet anode containing single cell has the highest ohmic resistance value 3.0 Ω cm^{-2} at 873 K (determined by the high-frequency intercept with the real axis in the Nyquist plot) (Figure 8a). Relatively high R_Ω value is presumed for the electrolyte supported design where the electrolyte layer is noticeably thick 725 μm for the ES Ni-cermet anode containing single cell. Anode supported Ni-cermet anode containing single cell (Ni-cell 2) has the thinnest electrolyte layers (for our systems ScSZ6 and GDC10 layers are both ~15μm thick, Figure 5a), nevertheless R_Ω values are still relatively high, for example 0.9 Ω cm^{-2} at 873 K (Figure 8b), compared to these presented in the literature [35]. Explanations to this could be the fact that the electrolyte layers are still comparably thick and not very well sintered due to comparatively low sintering temperature applied for preparation of single cells studied [3,65], or by poor homogeneity of raw NiO-GDC10 mixture, causing lack of effective electron and oxide ion pathways, as well as length of TPBs inside the anode. In addition, the reaction between ceria and zirconia during the sintering at 1623 K, leading to the formation of less conductive ScSZ|GDC or ScSZ|Ni-GDC interlayer, is probable [II]. The measured R_Ω values are the lowest for the electrolyte supported LSV30-cermet anode consisting single cell configuration (LSV-cell 4), for example: 0.8 Ω cm^{-2} at 873 K (Figure 8c), and are also in a good agreement at all measured temperatures with values calculated for a 130 μm thick SDC15 electrolyte (Figure 5a) from tabulated conductivities for SDC [8]. Also the open circuit voltage (OCV) values of ES LSV30-cermet anode containing single cells (LSV-cell 4) are relatively high, 1.00 V, 0.97 V and 0.94 V at 773 K, 823 K and 873 K, respectively. However, the obtained OCVs are somewhat lower than the calculated theoretical values of 1.154 V, 1.146 V, and 1.138 V, indicating the weak mixed conductivity effect of SDC15 under reducing conditions (i.e. the slight short-circuiting of the anode and cathode). Thus, they are still sufficiently high [8,56,79–81] to conclude that the electrolyte was gas leak tight [II].

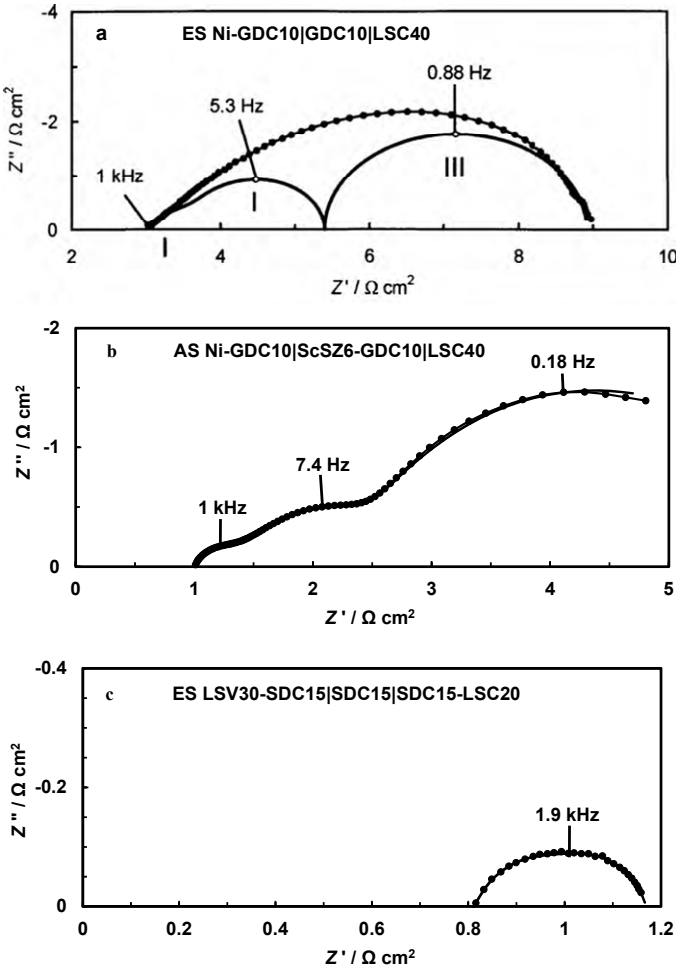

Figure 8. Nyquist plots at 873 K and open circuit voltage for a) ES Ni-GDC10|GDC10|LSC40 single cell (humidified fuel: H_2 at partial pressure 0.1 bar, oxidant: O_2 at partial pressure 0.2 bar), b) AS Ni-GDC10|ScSZ6-GDC10|LSC40 cell (Ni-cell 2) (humidified fuel: H_2 at partial pressure 0.2 bar, oxidant: O_2 at partial pressure 0.2 bar), and c) ES LSV30-SDC15|SDC15|SDC15-LSC20 cell (LSV-cell 4) (humidified fuel: H_2 at partial pressure 0.2 bar, oxidant: air). Filled symbols denote experimental data, black lines are fits using equivalent circuit I (a), II (b), and III (c) (the corresponding equivalent circuits are given in Figure 3).

For Ni-cermet anodes containing single cells, the polarization resistance values measured at 873K are similar: 6.0 Ω cm^{-2} for the electrolyte supported single cells (Figure 8a) and 5.5 Ω cm^{-2} for the anode supported single cells (Figure 8b). However, the characteristic frequency values are somewhat higher for electrolyte supported Ni-cermet anode containing single cell (Figure 8a and 8b). Therefore, it can be said that the Ni-cermet anode containing single cells performance did not depend noticeably on the geometry of the single cell

design. However, the LSV30-cermet anode containing cells show the lowest polarization resistance values: only 0.4 Ω cm^{-2} at 873 K (Figure 8c).

Influence of the cell potential on the shape of the Nyquist plots, i.e., on the electrochemical parameters of the single cell, is shown in Figure 9. The polarization resistance for the Ni-cermet anode containing single cells decreases with the potential applied. In addition, for anode supported cell configuration the decrease in the polarization resistance for all three semicircles is linear as demonstrated in Figure 10a. Dependence of the polarization resistance on the cell potential indicates that the slowest process is the charge transfer stage [I, II]. In Figure 9a it can also be seen that characteristic frequencies of the high-frequency process, f_{max1}, and for medium-frequency process, f_{max2}, decrease with the ΔE. The characteristic frequency of low-frequency process, f_{max3}, increases slightly with the decrease of the cell potential ΔE applied [II].

In the case of LSV30-cermet anode containing single cells the main response to the cell potential seems to arise due to the ohmic resistance, while the medium and low frequency polarization resistances are practically independent of current density, j, applied (Figure 9c). Based on the analysis of the fitting results of impedance spectra, there is a noticeable increase in the high-frequency series resistance with the decrease in j applied (Figure 10b). The medium-and low-frequency polarization resistances (i.e., charge transfer resistances at meso-porous and micro-porous areas, respectively) are nearly independent of j applied (Figure 10b). The reasons for some changes in ohmic resistance were not investigated in detail, however, the changes were found to be reversible (once the current flow was stopped, the ohmic resistance decreased back to the original value) [III], indicating that there is no degradation of cell component under study. Increase in R_Ω is mainly caused by the adsorption of the reaction intermediates onto the catalytically active centers of the anode.

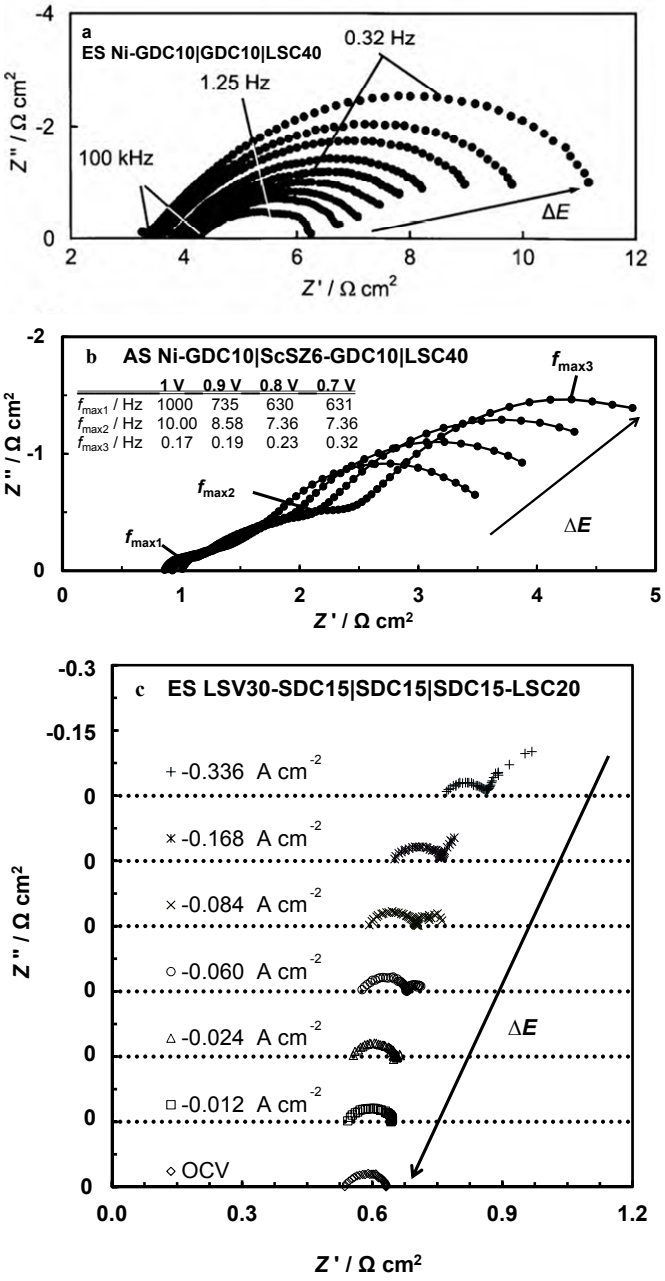

Figure 9. Nyquist plots at 873 K and at various cell voltages (the direction of increase of Δ*E* is shown in the Figure) a) ES Ni-GDC10|GDC10|LSC40 single cell (humidified fuel: H_2 at partial pressure 0.1 bar, oxidant: O_2 at partial pressure 0.2 bar), b) AS Ni-GDC10|ScSZ6-GDC10|LSC40 cell (Ni-cell 2) (humidified fuel: H_2 at partial pressure 0.2 bar, oxidant: O_2 at partial pressure 0.2 bar), and c) ES LSV30-SDC15|SDC15|SDC15-LSC20 cell (LSV-cell 4) (humidified fuel: H_2 at partial pressure 1 bar, oxidant: air).

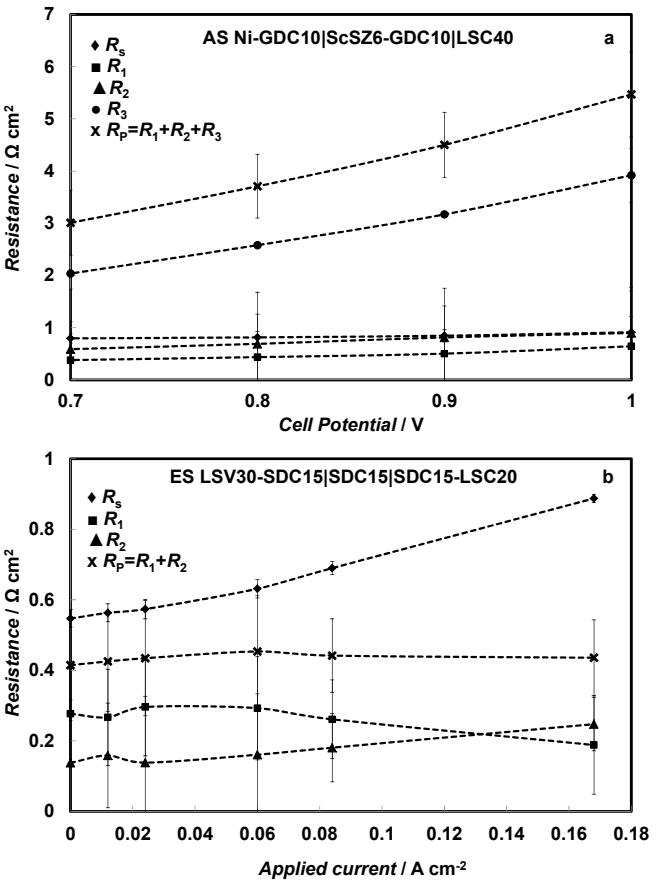

Figure 10. Resistance values (obtained by fitting) vs. cell potential data where R_s is the high-frequency series resistance, R_1 the resistance of the first semicircle, R_2 the resistance of the second semicircle, R_3 the resistance of the third semicircle, and R_P the polarization resistance.

The polarization resistance of the SOFC single cells studied decreases with working temperature. Figure 11a shows that characteristic frequency f_{max} (frequency of a maximum in the Z′, Z′′ plots) for three semicircles, established for supportive Ni-cermet anode consisting single cells, increases with the testing temperature applied, especially for high-frequency (1000–10000 Hz) and low-frequency (0.1–1 Hz) processes. Hence, nature of the rate-determining processes changes from the mixed kinetic process at T= 773 K (high-frequency process) towards the purely charge transfer limited process at T= 1023 K [86]. It is interesting that the medium-frequency mixed kinetic process is practically independent of the temperature applied. There is no noticeable dependence of the ratio between mass transfer and charge transfer limited steps, but there are noticeable changes in the total rate of the mixed-kinetic processes with temperature applied [II,IV].

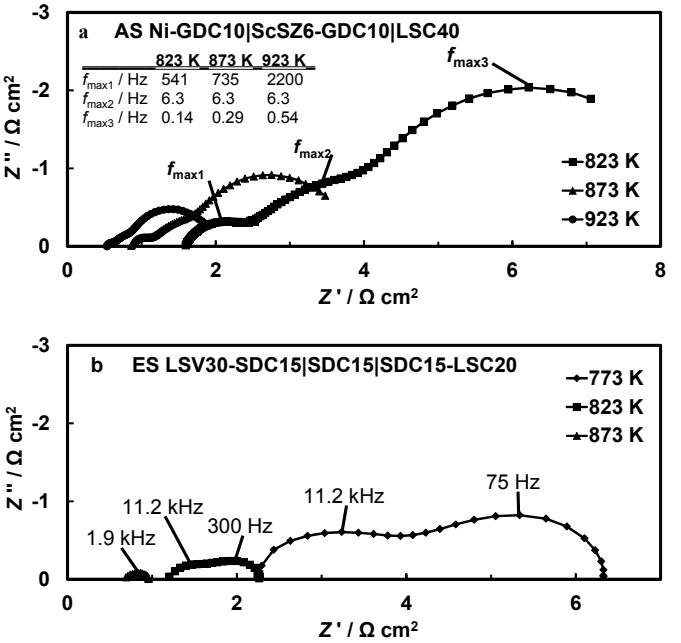

Figure 11. Nyquist plots at various temperatures (shown in the Figure) a) AS Ni-GDC10|ScSZ6-GDC10|LSC40 cell (Ni-cell 2), and b) ES LSV30-SDC15|SDC15|SDC15-LSC20 cell (LSV-cell 4). Humidified fuel: H_2 at partial pressure 1 bar, oxidant: O_2 at partial pressure 0.2 bar.

The polarization resistance for the LSV30-cermet anode containing single cell decreases with temperature from 4.1 Ω cm^2 to 0.3 Ω cm^2 at 773 K and 873 K, respectively (Figure 11b). It is noteworthy that the measured R_P for the studied cell at 873 K is comparable to that of a cell with a comparable anode composition, prepared into a porous YSZ8 scaffold, however measured at 100 K higher temperature (973 K) [32]. This difference between LSV30-YSZ8 and LSV30-SDC15 ceramic anode activities can be explained by the significantly higher ionic conductivity of SDC15 material, compared to YSZ8, at 873 K, which shows that the electrochemically active region of the electrode extends from the electrolyte|anode interface over the inner surface areas. It is furthermore interesting that the ionic conductivity for SDC15 at 873 K (0.019 S cm^{-1}[8]) is almost identical to that for YSZ8 at 973 K (0.018 S cm^{-1}[8]), suggesting that the comparable electrochemical performance can be mainly related with the ionic conductivity of the composite electrodes and only partially, for example, with the different chemical composition of the cathode materials applied [III].

6.1.1. Analysis of impedance spectra [Papers I, II, IV]

In order to investigate further the processes inside the SOFC electrodes, a new method called as the analysis of difference in impedance spectra (ADIS) has been used. ADIS can be used to deconvolute the single cell electrochemical response into anodic and cathodic processes contributions. It was found that this method can be used for Ni-cermet anodes containing single cells, because for LSV30-cermet anode containing single cells the difference of impedance spectra upon the fuel partial pressure or cell potential changes were too small.

Comparison of the $\Delta\partial Z'$ vs. log$f$ plots (Figure 12a) and $\Delta\partial Z''$ vs. log$f$ plots (Figure 13a) for electrolyte supportive Ni-cermet anode containing single cell upon hydrogen partial pressure and oxygen partial pressure variation experiments, and $\Delta\partial Z'$ vs. log$f$ plots upon cell potential variation experiments (Figure 14a) suggest that the process of highest characteristic frequency ($f_{max}\approx5$ Hz) corresponds to an anodic process, whereas the lower frequency process ($f_{max}\approx0.8$ Hz) can be assigned to the electroreduction of O_2, i.e. cathodic processes [13–15,94]. Therefore, the differences in corresponding derivatives established for single cells studied characterize the oxidation or reduction processes with different characteristic relaxation time constants. Furthermore, the values of the characteristic relaxation frequency for the single cells obtained using equivalent circuit modeling method (Figure 3 I) are in an excellent agreement with the characteristic relaxation frequency values obtained applying the$\Delta\partial Z'$ vs. log$f$ plot analysis (Figure 8a). However, it should be noted that the difference between f_{max} values established is quite low and the exact separation of the anode and cathode processes contribution for total impedance is complicated [86,93,95,99].[I]

From data in Figures 12b and 13b it follows that three processes influenced by the anode gas composition for supportive Ni-cermet anode containing single cell (Ni-cell 2) can be observed. The quickest process at frequencies from 10 to 10000 Hz (first semicircle) can be ascribed to dissociative adsorption of H_2 and transport to the three phase boundaries [93,96]. The second process at frequencies from 1 to 10 Hz (area between second and third semicircle) can be likely connected to the gas-phase diffusion limited step [97]. The slowest process within frequencies from 0.1 to 1 Hz (third semicircle) is most likely related to the fuel gas conversion and/or H_2O desorption from microporous Ni-catalytic sites [98].[II, IV]

The O_2 partial pressure influences the supportive Ni-cermet anode containing single cell impedance at frequencies from 20 to1000 (first semicircle), from 1 to 20 Hz (second semicircle) and from 0.5 to 5 Hz (third semicircle) (Figure 12b and 13b), likely corresponding to the dissociative adsorption of O_2 at higher frequencies that is followed the by electrochemical reduction and transfer of changed oxygen species at the tthree-phase boundary at lower frequencies [92,94,99]. Characteristic frequencies for cathodic processes obtained by oxygen variation method are comparable with the characteristic frequencies obtained by changing the cell potential (Figure 14b), where

the frequency regions from 10 to 100 Hz and from 0.1 to 1 Hz depend on the cell potential noticeably. [III, IV]

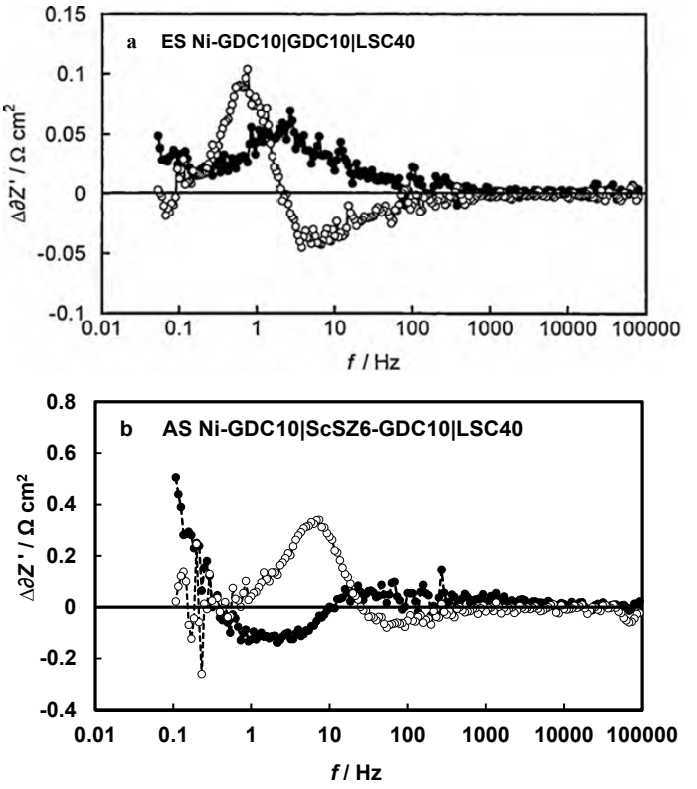

Figure 12. $\Delta\partial Z'$ vs. log$f$ plots for a) ES Ni-GDC10|GDC10|LSC40 single cell and, b) AS Ni-GDC10|ScSZ6-GDC10|LSC40 single cell (Ni-cell 2) upon gas composition variation conditions. Closed symbols correspond to the fuel variation experiment, $\Delta\partial Z'_{anodic}$, i.e. characterize a hydrogen partial pressure shift a) from 0.1 to 1 bar, and b) from 0.2 to 0.5 bar in humidified fuel in the anode compartment at a constant oxidant composition. Open symbols correspond to the oxidant variation experiment, ,$\Delta\partial Z'_{cathodic}$, i.e. characterize a oxygen partial pressure shift from a) from 0.2 to 1 bar, and b) from 0.2 to 0.5 bar in the cathode compartment at a constant fuel composition. All measurements were conducted at open circuit conditions at 873 K.

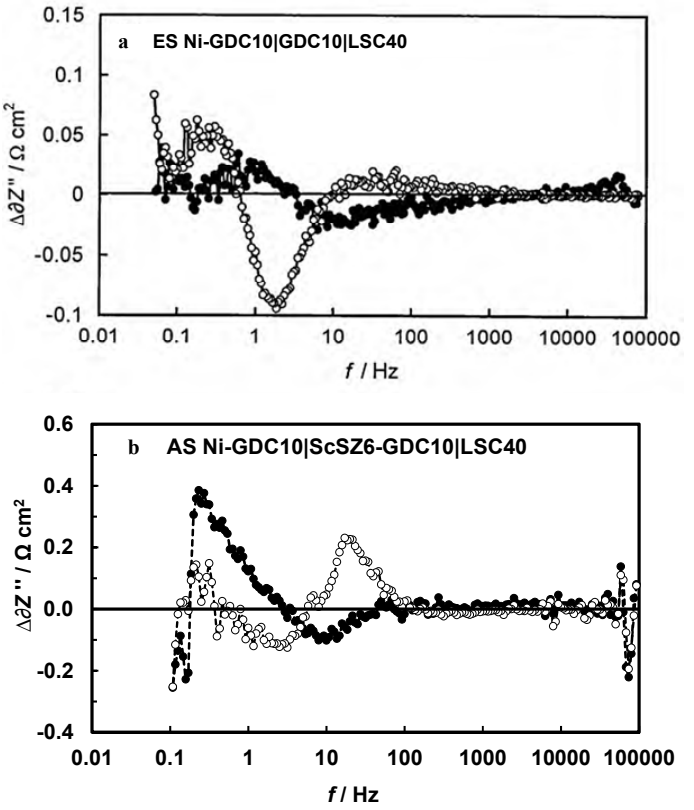

Figure 13. $\Delta\partial Z''$ vs. log$f$ plots for a) ES Ni-GDC10|GDC10|LSC40 single cell and, b) AS Ni-GDC10|ScSZ6-GDC10|LSC40 single cell (Ni-cell 2) upon gas composition variation conditions. Closed symbols correspond to the fuel variation experiment, $\Delta\partial Z'_{\text{anodic}}$, i.e. characterize a hydrogen partial pressure shift a) from 0.1 to 1 bar, and b) from 0.2 to 0.5 bar in humidified fuel in the anode compartment at a constant oxidant composition. Open symbols correspond to the oxidant variation experiment, ,$\Delta\partial Z'_{\text{cathodic}}$, i.e. characterize a oxygen partial pressure shift from a) from 0.2 to 1 bar, and b) from 0.2 to 0.5 bar in the cathode compartment at a constant fuel composition. All measurements were conducted at open circuit conditions at 873 K.

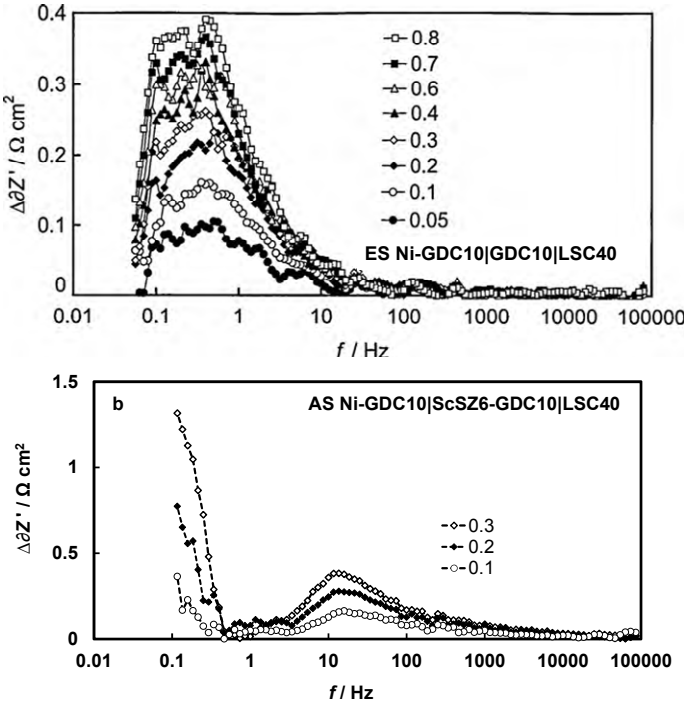

Figure 14. $\Delta\partial Z'$ vs. log$f$ plots for a) ES Ni-GDC10|GDC10|LSC40 single cell, and b) AS Ni-GDC10|ScSZ6-GDC10|LSC40 single cell (Ni-cell 2) upon cell potential variation. Difference between E_{OCV} and E_{fix} (fixed cell voltages) are noted in the figure. All measurements were conducted at constant H_2 and O_2 partial pressure conditions at 873 K.

The fitting data of Nyquist spectra for supportive Ni-cermet anode containing single cell (Ni-cell 2) at 873 K at different fuel and oxygen partial pressures are presented in Table 3, establishing that increasing the partial pressure of hydrogen decreases the polarization resistance of the first high-resistance semicircle, while the polarization resistance of the second (so-called middle-frequency) semicircle decreases noticeably with increasing the oxygen partial pressure in the oxidant compartment. The polarization resistance of the third very low-frequency semicircle decreases with the increase of the partial pressure of hydrogen in the fuel compartment and also with the partial pressure of oxygen in the oxidant compartment. This indicates that the first semicircle corresponds most likely to the anodic processes while the second semicircle is mainly influenced by the cathodic process. The low-frequency polarization resistance (i.e. the wideness of the third semicircle in impedance spectra) is influenced by both anodic and cathodic slow rate processes. Information gathered from fitting of the experimental curves is in good agreement with ADIS method. [II]

Table 3. Fitting data for Nyquist plots at open circuit voltage and at different gas partial pressures (given in the table) for Ni-cell 2 at 873 K.

	0.2 bar H_2 0.2 bar O_2	0.2 bar H_2 0.5 bar O_2	0.5 bar H_2 0.5 bar O_2	0.5 bar H_2 0.2 bar O_2
R_s / Ω cm^{-2}	0.914(2)	0.844(1)	0.860(1)	0.879(1)
R_1 / Ω cm^{-2}	0.64(1)	0.577(7)	0.6146(8)	0.5452(5)
R_2 / Ω cm^{-2}	0.91(2)	0.678(7)	0.754(9)	1.025(9)
R_3 / Ω cm^{-2}	3.9170(5)	3.4850(5)	3.1320(4)	3.2330(5)
R_P / Ω cm^{-2}	5.471	4.839	5.5008	4.803
f_{max1} / Hz	584	736	100	584
f_{max2} / Hz	7.94	18.48	13.94	7.36
f_{max3} / Hz	0.711	0.185	0.215	0.200

Comparison of the ADIS spectra for Ni-cermet anode containing electrolyte supported cell with those for the anode supported cell demonstrates that some differences in the characteristic maximum frequencies of the processes appeared. Anodic processes for the electrolyte supported cell are slightly shifted towards the higher frequencies and the cathodic processes towards lower frequency region. It should be remembered that the frequency ranges discussed for the anodic and cathodic processes partially overlap, so precise separation and identification of oxidation and reduction processes is extremely difficult. Furthermore, changes in the data for anode or cathode influence the potential of the other electrode and therefore we can see the mixed contribution of the both processes to the ADIS spectra.

6.2. Influence of the supportive Ni-GDC cermet anode microstructure on the SOFC single cell performance [Papers II, IV]

Supportive Ni-cermet anodes have very well developed hierarchical porous structures (Figure 15). The pore volume fraction values (calculated according to Equation 1) for non-reduced anode structure increase from 9.8 to 13.1 with increasing the pore former (graphite no. 1, Figure 4) amount from 1 wt% to 4 wt% in the anode raw material (Table 1). The same tendency can also be observed in the case of mercury intrusion porosimetry data, for reduced Ni-cermet anodes. The total porosity of the Ni-cermet anode increases from 34.2% to 40.8% (Table 1) with increasing the pore former content from 1 wt% to 4 wt% in the anode raw material. These data are also consistent with FIB-SEM images (Figure 15).

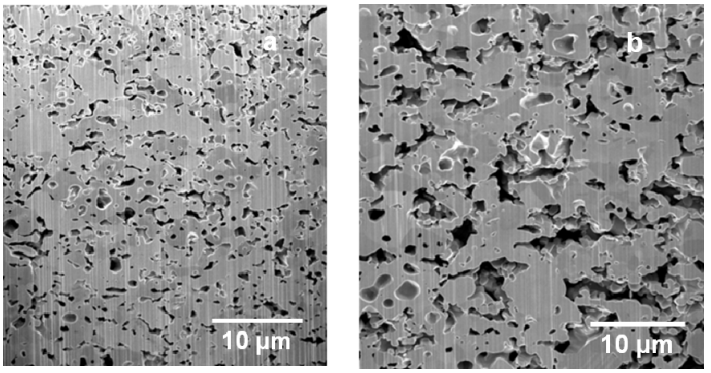

Figure 15. FIB-SEM images of Ni-GDC10-cermet anode materials with a) no pore former and b) 4 wt% pore former no. 1 in anode raw material.

On the other hand, no significant dependence of *PVF* for non-reduced anode on the pore former particle size in the anode raw material can be detected (Table 1) due to the dispersion and overlapping of the pore former particle size distribution (Figure 4) functions for different graphites used. However, according to the mercury intrusion porosimetry measurement data, the pore size distribution function maximum shifts slightly from 1.1 µm to 1.41 µm, if graphite no 1 and graphite no 5 were used as pore formers, respectively.

The values of maximum power density, P_{max}, for single cells were calculated using the cyclic voltammetry data (Equation 23). In Figure 16a it can be seen that P_{max} slightly increases with the increase of pore former amount in the anode raw material, being in an agreement with the literature data for SOFCs based on YSZ electrolyte [65]. For single cell with the optimized porosity of the anode, tested at temperature 873 K in 0.2 bar humidified H_2 and 0.2 bar O_2, approximately 30% higher P_{max} value of 92 mW cm^{-2} was obtained compared with non-optimized anodes (P_{max}=27 mW cm^{-2}). At higher temperatures the increase in P_{max} is slightly smaller. However, no remarkable dependence of P_{max} on the particle size of the pore former in the anode raw material is established (Figure 16b).

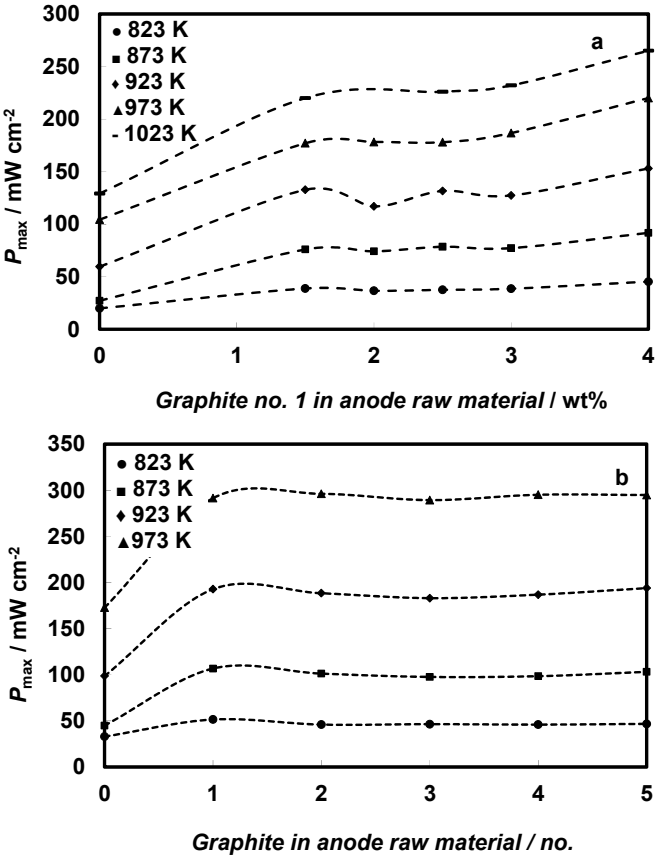

Figure 16. Maximum power density data measured at different temperatures (noted in Figure) at open circuit voltage a) at different wt% of the pore former and b) for the different pore formers with the different particle size distribution in the anode raw material (a) humidified fuel: H_2 at partial pressure 0.2 bar, oxidant: O_2 at partial pressure 0.2 bar b) humidified fuel: H_2 at partial pressure 0.2 bar, oxidant: O_2 at partial pressure 1 bar).

The values of polarization resistance, R_P, were obtained from the impedance spectra by fitting the calculated spectra to experimental ones (using equivalent circuit shown in Figure 3 II) to estimate the resistance of high-, medium- and low-frequency processes separately. Data in Figure 17 show that R_P slightly decreases with increasing the pore former amount and with decreasing the pore former particle size in the anode raw material. The activation energy values were calculated using the values of R_P established. It is estimated that the activation energy decreases from 1.25 eV to 1.09 eV with increasing the pore former amount from 0 wt% to 4 wt% in the anode raw material, respectively. However, no noticeable dependence of the activation energy on the pore former particle size distribution is detected.

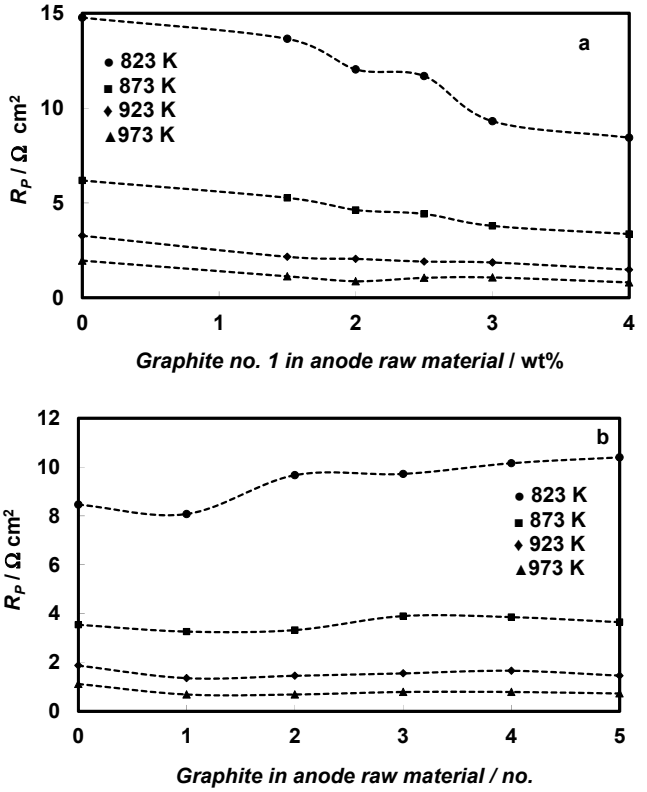

Figure 17. Polarization resistance data measured at different temperatures (noted in Figure) at open circuit voltage a) at different wt% of the pore former and b) for the different pore formers with the different particle size distribution in the anode raw material (a) humidified fuel: H_2 at partial pressure 0.2 bar, oxidant: O_2 at partial pressure 0.2 bar b) humidified fuel: H_2 at partial pressure 1 bar, oxidant: O_2 at partial pressure 1 bar).

The ADIS spectra were constructed to determine the frequency ranges that had been mainly influenced by the anode structure. It has been found that the pore former wt% in the anode raw material influences the Nyquist plot shape. Slight influence is seen at the high-frequency (from 20 to 1000 Hz i.e., the first semicircle) corresponding to the dissociative adsorption of H_2 and transport to the three phase boundary. Quite significantly influence is seen at the medium-frequency range (with the maximum at 11 Hz) limited by the gas diffusion step. The most significant influence is seen at the low-frequency process (from 0.1 to 1 Hz, i.e., the third semicircle) (Figure 18a) determined by the rate of the fuel conversion and/or H_2O desorption from the microporous Ni-catalytic sites. The pore former particle size distribution in the anode raw material has bigger influence on the medium-frequency process (within the frequency range from 3 to 10000 Hz, i.e., the first and second semicircle) (Figure 18b) compared with the influence of the amount of the pore former.

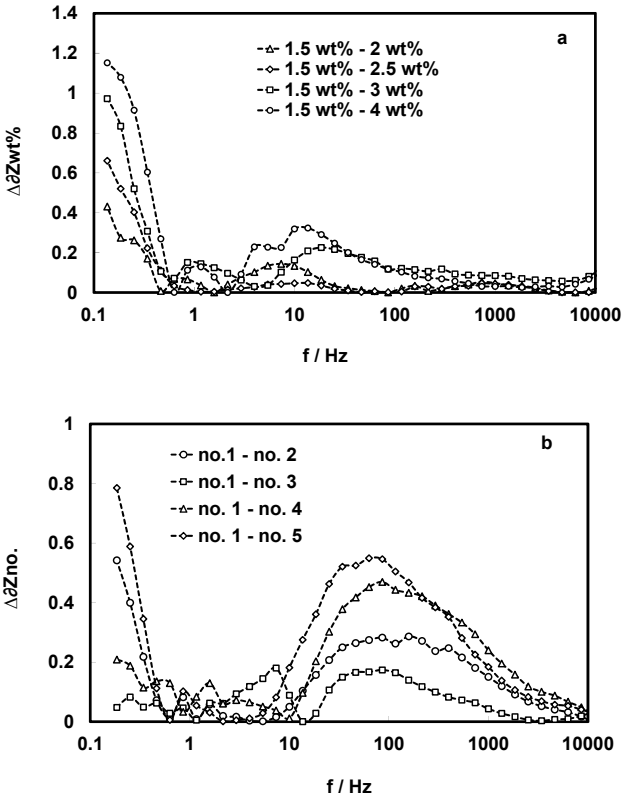

Figure 18. $\Delta\partial Z$ vs. log$f$ plots a) for variation of the graphite no. 1 amount in the anode raw material, and b) for variation of the pore former particle size in the anode raw material, measured at temperature 872 K and at open circuit voltage. Humidified fuel: H_2 at partial pressure 0.2 bar, oxidant: O_2 at partial pressure 0.2 bar.

Effects demonstrated in the Figure 18, were confirmed by the results of the fitting analysis of the Nyquist plots. It can be seen in Figure 19 that there is a noticeable decrease in the polarization resistance with increasing pore former amount in the supporting anode raw material. It has also been observed that the characteristic frequency for the third semicircle, f_{max3}, increases with the supporting anode porosity. This indicates that the gas conversion and/or H_2O desorption from the microporous Ni-catalytic sites is more effective due to increased pore volume fraction (Table 1) of the supporting anode. Figure 20 shows that the resistance obtained by the wideness of the first and the second semicircles (R_1+R_2), increases with the pore former particle size, while the resistance for the low frequency processes, R_3, (wideness of the third semicircle) decreases. Thus, the gas diffusion rate through the anode with the larger pore sizes increases. However, it seems that the gas conversion activity at three-phase boundaries is slower.

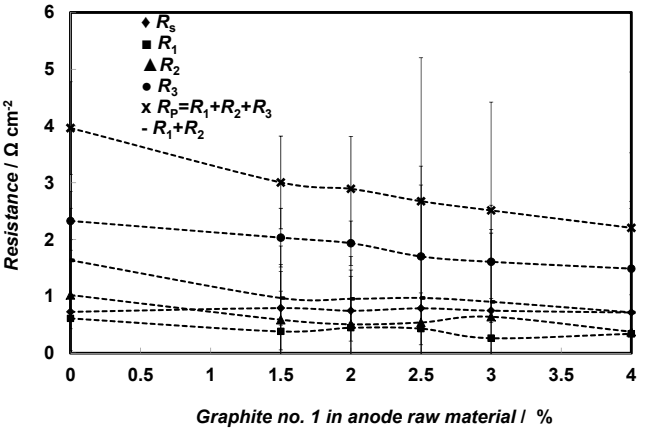

Figure 19. Dependence of the resistance (obtained using the fitting) on the pore former amount in the anode raw material, measured at temperature 872 K and at open circuit voltage. Humidified fuel: H_2 at partial pressure 0.2 bar, oxidant: O_2 at partial pressure 0.2 bar.

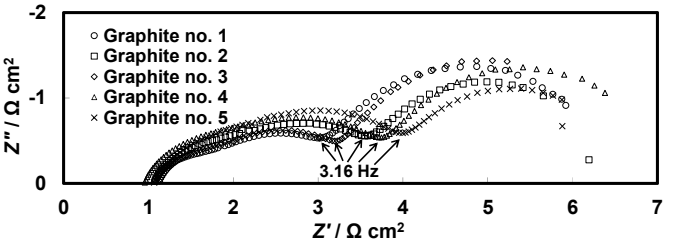

Figure 20. Nyquist plots for various anode supported single cells prepared using the different pore formers with different particle size distributions in the anode raw material, measured at temperature 872 K and at open circuit voltage. Humidified fuel: H_2 at partial pressure 0.2 bar, oxidant: O_2 at partial pressure 0.2 bar.

6.3. Influence of the ceramic LSV30-SDC15 anode microstructure on the SOFC single cell performance [Papers III, V]

Five LSV30-SDC15 cermet anodes with different microstructures of the porous SDC15 scaffold have been characterized and investigated (Table 2). Firstly, the influence of the SDC15 scaffold surface roughness, achieved by wet etching with HF acid, was examined. Secondly, the influence of the porosity and the pore size distribution of the SDC15 scaffold were manipulated using different pore formers in the porous SDC15 green tape.

For LSV-cells 1–5 (Table 2) the synthetic graphite from Alfa Aesar (300 mesh), graphite no. 6, was used as a pore former in the porous SDC15 green tape. The porosity of the blank SDC15 scaffold, calculated from the weight

change upon immersion it into the boiling water (based on three identical slabs tested at least for 5 times), is found to be approximately 60%. This value is slightly smaller than that obtained for YSZ8 scaffolds prepared using nearly identical procedures [32]. It is found that the pores in the empty porous SDC15 matrix are uniformly distributed within the range from 1 μm to 2 μm (Figure 21a) and the specific surface area of the scaffold is of 0.32 m^2 g^{-1} (based on BET isotherms data measured using Kr adsorption at 78 K). After etching the empty porous SDC15 scaffold with concentrated HF acid aqueous solution for 1 h at room temperature, the specific surface area of the SDC15 scaffold increased up to 0.53 m^2 g^{-1}. This increase is smaller than has been observed for YSZ8 scaffolds (from 0.48 m^2 g^{-1} to 2.1 m^2 g^{-1} [73]) under comparable conditions. The smaller increase in specific surface area for the SDC15 scaffold after applying HF-treatment can be explained by the resulting electrolyte microstructure. For YSZ8, HF-treatment lead to a complete restructuring of the electrode surface structure, the entire pore network was changed into sheet- and pillar-like structures [73]. In the case of SDC15, the increase in specific surface area is only due to the generation of higher SDC15 surface roughness (Figure 21) because of the different solubility of Ce^{4+} ions and Zr^{4+} ions in the water phase [75]. From Figure 21b it can be seen that the depth of the etching of SDC15 with HF acid is only ~0.1 μm and the increase of the specific surface area has been calculated to be ~37%. These data are in a good agreement with Rupp et al results [76].

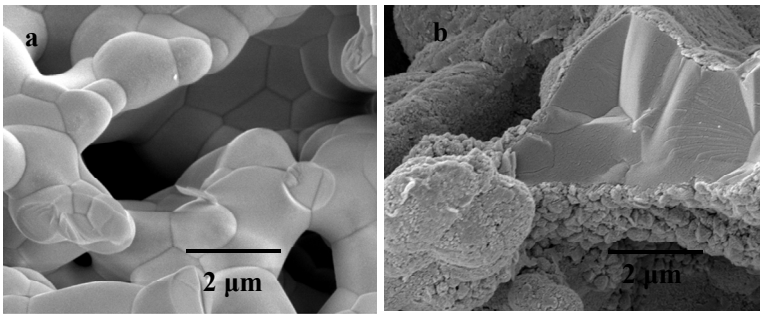

Figure 21. SEM micrographs of ~60% porous SDC15 scaffold a) without HF-treatment and b) after HF treatment.

For LSV-cells 6–8 (Table 2), three different graphite materials with different particle size distributions were used as pore formers in the porous SDC15 green tape. 3D microstructure images for these three different porous SDC15 scaffolds before the infiltration step, obtained via FIB-SEM method, are shown in Figure 22. The most porous SDC15 scaffold with 75% porosity was prepared using graphite no. 3 as a pore former (Figure 22a). This porous SDC15 structure is also the most micro-heterogeneous with the average SDC15 particle size 850 nm (Figure 23a) and with the highest average pore size of 2200 nm (Figure 23b). However, this structure has the lowest specific surface area, 0.53 μm^2 μm^{-3}.

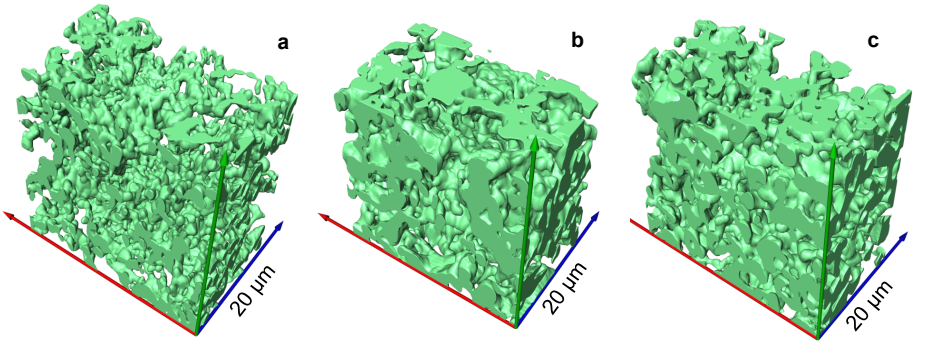

Figure 22. the 3D images for the porous SDC15 scaffolds, if a) graphite no. 3, b) graphite no. 5, and c) graphite no. 7 have been used as pore formers.

The structures of the porous SDC15 scaffolds, prepared using graphite no. 5 or graphite no. 7 as pore formers seem to be quite similar (Figures 22b and 22c). The total porosity values calculated from FIB-SEM data are 60% and 57%, respectively, and average SDC15 particle sizes are 1200 nm and 1275 nm (Figure 23b), respectively. However, there are some small differences in these seemingly comparable microstructures (Figures 22b and 22c). The porous SDC15 scaffold obtained by using graphite no. 5 as a pore former has the average pore size of 2000 nm (Figure 23b) and the specific surface area 0.54 $\mu m^2\ \mu m^{-3}$. These values are comparable with the porous SDC15 structure if graphite no. 3 was used as a pore former. The porous SDC15 scaffold prepared using the pore former graphite no. 7 has the highest specific surface value, s_A= 0.64 $\mu m^2\ \mu m^{-3}$, but the lowest average pore size value, d_{pore}=1550 nm. Also, this structure does not seem to have any macro-pores. Therefore, for the electrochemical testing, three different porous SDC15 scaffolds have been prepared: 1) sample with the high porosity and with the average pore sizes (Figure 22a), 2) sample with the average porosity and with the average pore sizes (Figure 22b), and 3) sample with the average porosity, but with the small pores (Figure 22c).

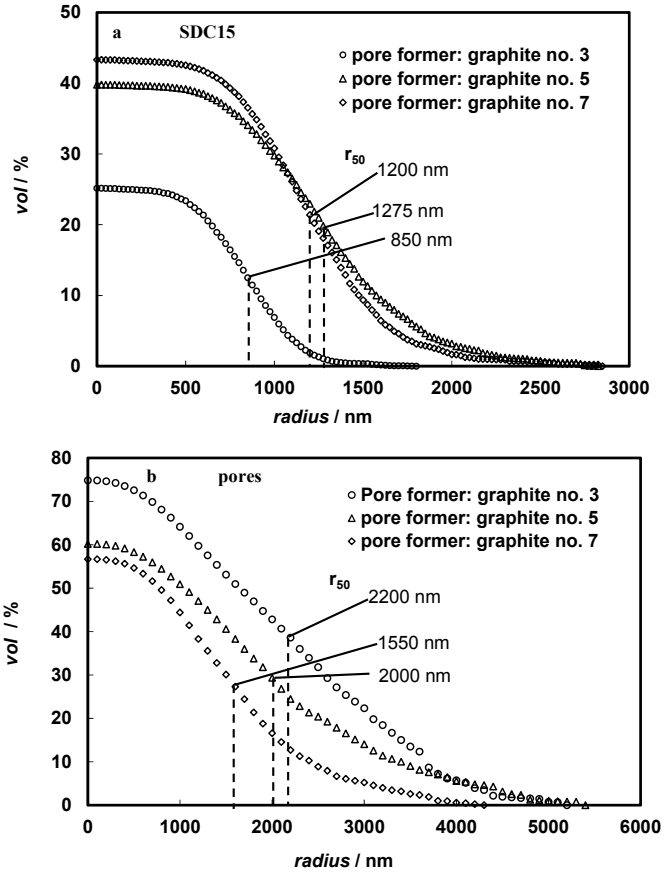

Figure 23. Particle size distribution data a) for SDC15 material and b) for the pores of the porous SDC15 scaffolds prepared and tested.

Into the porous SDC15 scaffolds 20 vol% of LSV30 (LSV-cell 1–5) or 10 vol% of LSV30 (LSV-cell 6–8) was deposited using infiltration and there after sintered at 973 K. Figure 24 shows that LSV30 does not form a uniform film over the SDC15 scaffold like it has been observed for YSZ8 scaffold [32]. This suggests that LSV30 interacts differently with SDC15 surface than with YSZ8 and probably leads to an increased concentration of the three-phase boundary sites in the LSV30-SDC15 composite.

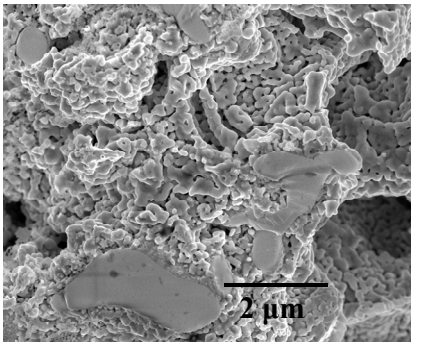

Figure 24. SEM micrograph of infiltrated LSV30 into the porous SDC15 scaffold (graphite no.6 was used as a pore former).

Park et al [32] have shown that $(La_{0.7}Sr_{0.3})VO_{3.85}$ powder, synthesized at 973 K in air, will be reduced (partially decomposed) into $(La_{0.7}Sr_{0.3})VO_{2.94}$ powder after reduction at 973 K in H_2 atmosphere. Measured X-ray diffractograms (Figure 25) show that the desired LSV30-SDC15 phase has been prepared. The peak characteristics for $Ce_{0.85}Sm_{0.15}O_{2-\delta}$ are observed at 28.5°, 33.0°, 47.3°, 56.2° and 58.9°, of unreduced $La_{0.7}Sr_{0.3}VO_{4-\delta}$ composite at 26.0°, 27.7°, 30.0° and 44.9° as well as of reduced $La_{0.7}Sr_{0.3}VO_{3-\delta}$ composite at 22.8°, 32.4°, 40.0°, 46.5° and 57.8° at 2θ values, identified by using ICDD-PDF-2-Relase2010 database. More detailed crystallographic analysis data is demonstrated in Figure 25 and is given in legend of the Figure 25.

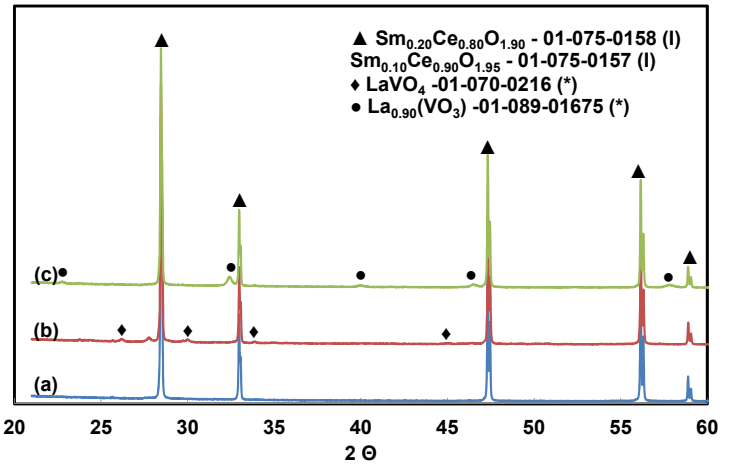

Figure 25. XRD patterns for a) $Ce_{0.85}Sm_{0.15}O_{2-\delta}$ porous scaffold; b) $La_{0.7}Sr_{0.3}VO_{4-\delta}$-$Ce_{0.85}Sm_{0.15}O_{2-\delta}$ composite; and c) $La_{0.7}Sr_{0.3}VO_{3-\delta}$-$Ce_{0.85}Sm_{0.15}O_{2-\delta}$ composite after reduction at 973 K for 5 h in H_2. ▲–peak characteristics for $Ce_{0.85}Sm_{0.15}O_{2-\delta}$; ♦–peak characteristics for $La_{0.7}Sr_{0.3}VO_{4-\delta}$-$Ce_{0.85}Sm_{0.15}O_{2-\delta}$, and ●–peak characteristics for $La_{0.7}Sr_{0.3}VO_{3-\delta}$-$Ce_{0.85}Sm_{0.15}O_{2-\delta}$.

It has been previously demonstrated for YSZ8 electrolyte based systems [31,32,50,55] that small amounts of CeO_2 and Pd are required in order to achieve good electrode performance with a number of ceramic conductors, including LSCM [50], LST [31,46], and LSV [32,50,73]. In Figure 26 the j vs. E dependence (so-called polarization curves, j-current density, E-cell potential) and the corresponding power densities are presented for four differently completed cells: one with the ceramic anode only consisting of 20 vol% LSV30 infiltrated into the porous SDC15 scaffold (LSV-cell 1), for others systems the LSV30-SDC15 structure was additionally activated with catalysts i.e., 2.1 vol% of CeO_2 or 0.3 vol% of Pd or both (LSV-cell 2, LSV-cell-3, LSV-cell 4, respectively). All cells under comparison had the same cathodes, prepared by infiltrating the 25 wt% of LSC20 into the porous SDC15 scaffold. The results in Figure 26 show that the single cell without CeO_2 and Pd promoters exhibits very low catalytic activity towards H_2 oxidation, with a high R_P of 2.0 $\Omega \cdot cm^2$ and a low P_{max} of 17 mW cm^{-2} at 873 K. These results are comparable to the results established for single cells based on LSV30-YSZ8 composite anodes [32]. The single cell containing LSV30-SDC15 anode activated with 2.1 vol% of CeO_2 catalyst demonstrates only slightly better electrochemical performance (R_P=1.4 Ω cm^2 and P_{max}=25 mW cm^{-2} at 873 K). The replacement of CeO_2 with 0.3 vol% of Pd increases the electrochemical performance further: P_{max} increases to 59 mW cm^{-2}. However, P_{max} of the single cell containing anode activated with CeO_2 and Pd is significantly higher: 139 mW cm^{-2}, corresponding to an 8-fold increase in power density compared to the LSV30-SDC15 anode without promoters deposited into the anode surface. The R_P of the single cell with both CeO_2 and Pd nanoclusters at the LSV30-SDC15 anode is 0.3 $\Omega \cdot cm^2$. Thus, our results do not confirm the recent findings by Ciucci et al [58] and Chueh et al [59], suggesting that the electrochemical activity for ceria-supported metal anodes originates mainly from the ceria phase. Therefore, if it would be true, no enhancement in electrochemical performance should be observed when 0.3 vol% of Pd catalyst was added into the LSV30-SDC15 structure that was already activated with CeO_2. Furthermore, only a small increase in performance is observed with the addition of CeO_2 species alone into LSV30-SDC15 anode [III].

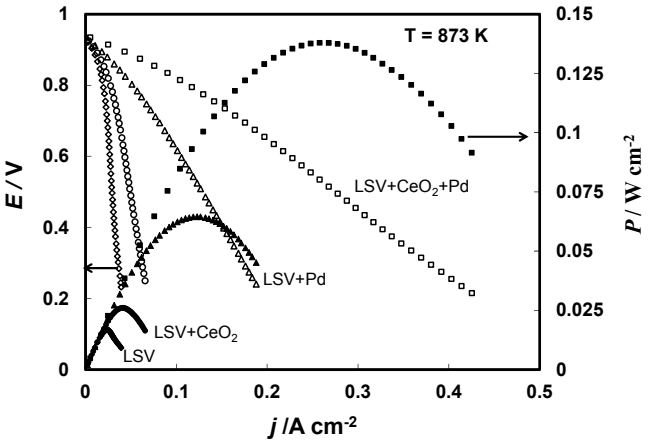

Figure 26. Cell potential and power density vs. current density curves for the $La_{0.7}Sr_{0.3}VO_{3-\delta}$–$Ce_{0.85}Sm_{0.15}O_{2-\delta}$ anode (◊) without catalysts, (○) with addition of 2.1vol% CeO_2, (Δ) with addition of 0.3 vol% Pd and (□) with addition of 2.1 vol% CeO_2 and 0.3 vol% Pd, at 873 K if humidified (3% H_2O) H_2 has been used as a fuel.

Therefore, all the electrochemical measurements for different LSV30-SDC15 anode microstructutres were obtained after adding CeO_2 and Pd as promoters/ catalysts into the LSV30-SDC15 anode side.

6.3.1. Influence of the SDC matrix surface area on the electrochemical performance of the single cell [Paper III]

At first, the influence of the bulk SDC15 scaffold surface roughness on the electrochemical performance has been investigated. It is seen that already the minor increase in specific surface area of the bulk porous SDC15 scaffold resulted in considerably better cell performance. In Figure 27 it can be seen that P_{max} increases ~1.7 times, from 140 mW cm^{-2} to 234 mW cm^{-2}, measured using humidified H_2 at 873 K. R_P value decreases from 0.3 Ω cm^2 to 0.1 Ω cm^2 at same measurement conditions. The HF-treated sample demonstrates considerably higher power densities in hydrogen atmosphere, however, the same single cell does not have noticeably better electrochemical performance in methane atmosphere (Figure 27). This can be explained that rate-limiting processes are slow diffusion of fuel or reaction products through the macro-mesopores to the reaction zone and, therefore, the effect of the modified microstructure of the electrode is unimportant. The corresponding values of P_{max} at 873 K are 101 mW cm^{-2} and 104 mW cm^{-2} for untreated and HF-treated single cells, respectively (Figure 24), and the corresponding R_P values are 0.6 Ω cm^2 and 0.4 Ω cm^2. These results are comparable with those for LSV30-YSZ8 anode consisting single cell in methane at 1073 K [32]. The lower electrochemical performance of the single cells operating with CH_4 as a

fuel, instead of H_2, is most likely due to the catalytic limitations for the breaking of the C-H bonds in the methane molecule.

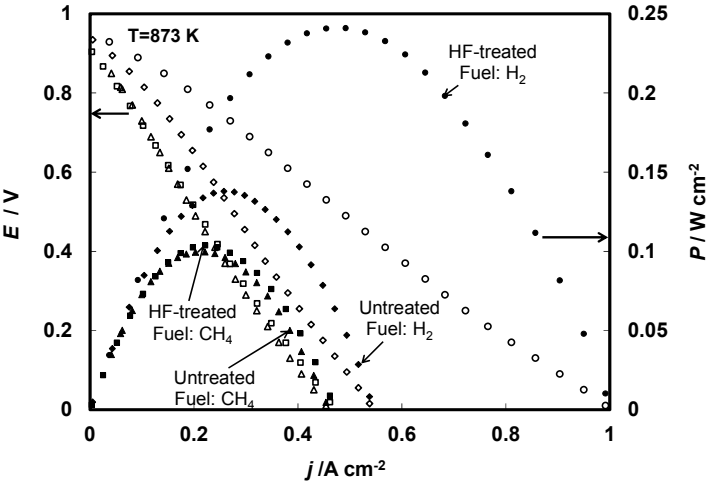

Figure 27. Cell potential and power density vs current density curves for the cells operated at 873 K and based on the porous scaffold that was (◊,Δ) untreated, and (○,□) HF-treated before infiltration. Fuels are (◊,○) humidified (3% H_2O) H_2 and (Δ,□) humidified (3% H_2O) CH_4.

Figure 28 shows stable operation of LSV-cell 5(i.e. HF-treated sample) under a current load of both humidified hydrogen (for 38 h) and in humidified methane (for 40 h). Low constant current densities, –0.114 A cm^{-2} and –0.096 A cm^{-2} have been applied for humidified hydrogen and methane, respectively, while measuring the system potential changes. Based on data in Figure 28, no significant degradation is observed during the testing periods. This suggests that the LSV30-SDC15 composite system is a promising candidate for Ni-free ceramic anodes for SOFCs, operating 873 K or below. After the long term operation at 873 K in humidified H_2 and CH_4, the LSV30-SDC15 anode surface was studied using SEM method and no detectable carbon formation on the electrode from CH_4 was observed. However, more systematic future microstructure optimization and mesoporosity development is required for completing the high power density SOFC based on the ceramic anodes.

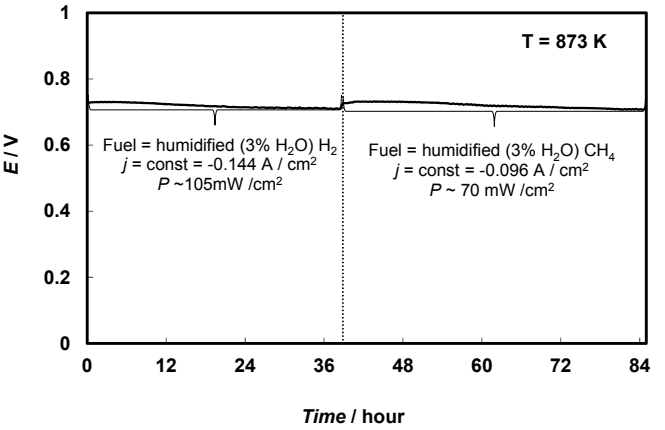

Figure 28. Cell potential vs. polarization time dependence under the constant current load of the LSV-cell 5 measured at 873 K if humidified (3% H_2O) H_2 and in humidified (3% H_2O) CH_4 has been used as fuels.

6.3.2. Influence of the SDC matrix porosity and pore size on the electrochemical performance of the single cell [Paper V]

Influence of the bulk SDC15 scaffold porosity and pore size distribution on the electrochemical performance of the SOFC single cell was investigated. It can be seen in Figure 29 that in the case of humidified hydrogen atmosphere the single cell LSV-cell 6 demonstrates the highest power density values: 200 mW cm^{-2} and 320 mW cm^{-2} at 823 K and 873 K, respectively. The least active single cell is LSV-cell 8 with P_{max} values of 111 mW cm^{-2} and 234 mW cm^{-2} at 823 K and 873 K, respectively. LSV-cell 7 demonstrates the medium electrochemical activity with P_{max} of 149 mW cm^{-2} and 275 mW cm^{-2} at 823 K and 873 K, respectively.

In the case of hydrogen fuel the electrochemical activity of the single cells depends noticeably on the porous SDC15 scaffolds microstructure, indicating that porosity and pore size distribution are very important parameters that determine the single cell performance. Firstly, the bigger pores and also the higher porosity allow the faster gas transportation into the electrochemically active centers. Secondly, the microstructure of the SDC scaffold may have some effect on the catalytic activity. SDC is known to obtain electrical conductivity in the hydrogen atmosphere [8]. Therefore, the finer is the SDC structure, the more extensive is the reduction of Ce^{4+} in the SDC electrolyte porous matrix. At these conditions the SDC porous matrix obtains mixed conductivity, like LSV, and it contributes to the increase of the active centers for the electrochemical reactions. However, if electric conductivity of the SDC electrolyte matrix increases, the ionic conductivity decreases, and the transport of the oxide ions may not be efficient. Thirdly, the higher specific surface area most likely increases the number of the catalytically active reaction sites.

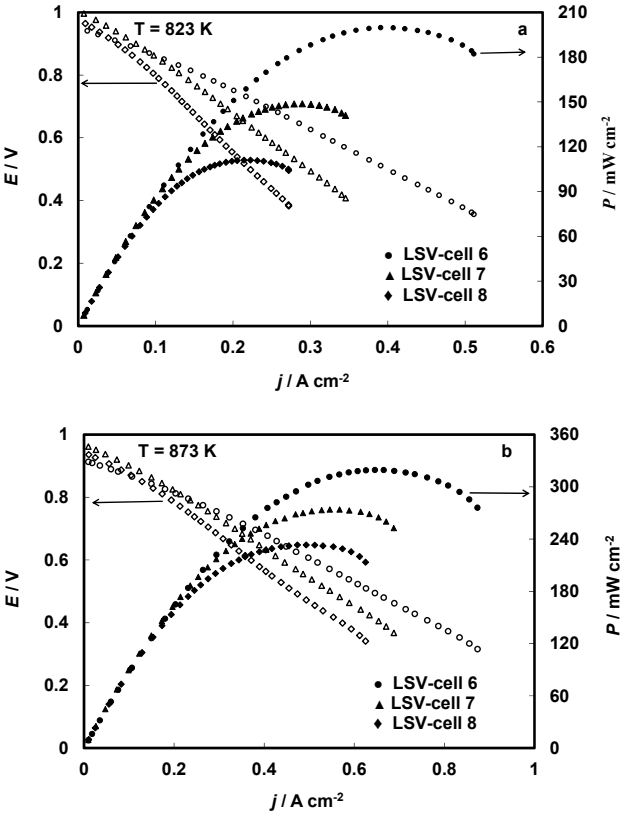

Figure 29. Cell potential and power density vs current density curves for three different solid oxide fuel cell single cells at a) 823 K and b) 873 K if humidified (3% H_2O) H_2 has been used as a fuel.

LSV-cell 6 has the highest porosity and the finest particle size of the SDC15 framework. Therefore, the porosity of the electrodes is sufficient for the quick gas transport and the partial reduction of SDC15 framework may contribute into the overall activity of the anode. The SDC15 porous scaffold for the LSV-cell 7 has the similar pore size distribution, but bigger SDC15 particles. As a result, the effect of SDC15 partial reduction is not so noticeable. LSV-cell 8 has the highest specific surface area, however, the electrochemical activity is the lowest. This effect can be explained by the formation of the closed pores in the microstructure during the infiltration process, mainly because of the smaller pore size distribution of the porous SDC15 scaffold. Therefore, the LSV-cell 8 has most likely the lowest concentration of active reaction centers compared to the LSV-cell 6 and LSV-cell 7.

It should be noted that the electrochemical activity of the single cells decreases approximately 50% if humidified methane is used instead of the humidified hydrogen as a fuel (Figure 30). One of the reasons for the lower electrochemical activity of the single cells with humidified methane atmosphere

is probably caused by the extra energy needed to break the chemical bond between C and H atoms in the methane molecule. In the humidified methane fuel conditions, LSV-cell 7 has the highest P_{max} values: 89 mW cm^{-2} and 175 mW cm^{-2} at 823 K and 873 K, respectively. LSV-cell 6 demonstrates only slightly lower P_{max} values (74 mW cm^{-2} and 161 mW cm^{-2} at 823 K and 873 K, respectively). LSV-cell 8 has the lowest activity also in humidified methane: P_{max} values are 60 mW cm^{-2} and 141 mW cm^{-2} at 823 K and 873 K, respectively.

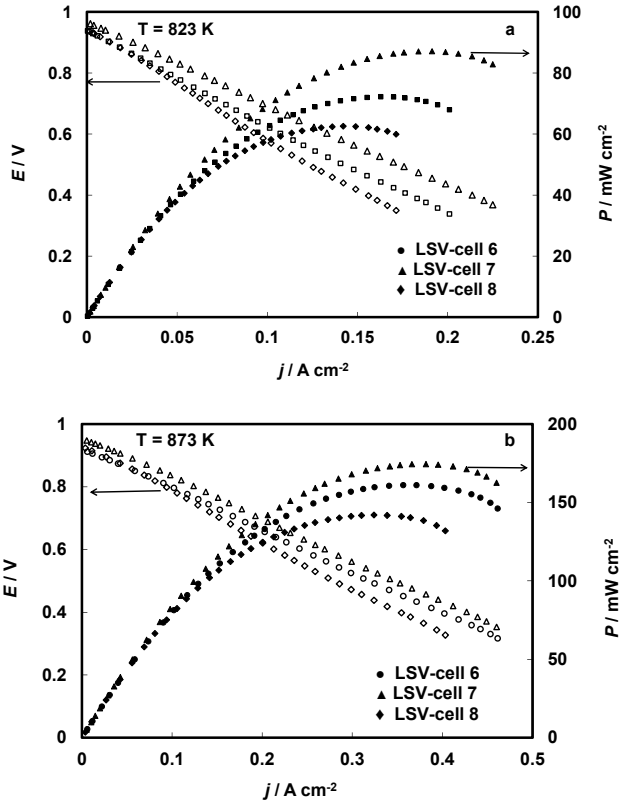

Figure 30. Cell potential and power density vs current density curves for three different solid oxide fuel cell single cells at a) 823 K and b) 873 K if humidified (3% H_2O) CH_4 has been used as a fuel.

One of the reasons for the LSV-cell 6 single cell worse performance in the case of methane, compared to the hydrogen, can be the less extensive partial reduction of the porous SDC15 framework. Analyzed data indicate that the performance of the single cell working with methane can probably be somewhat increased by increasing the hierarchical porosity and the concentration of the reaction sites in the anode, but keeping the porosity value somewhat lower than 75%. Most likely the 75% porosity of the porous SDC15 scaffold is too high and the amount of the SDC15 material in matrix is not sufficient to provide active centers with oxide ions at level for good SOFC single cell performance.

7. SUMMARY

Solid oxide fuel cell (SOFC) single cells with different design and configurations were prepared: electrolyte supported Ni-$Ce_{0.9}Gd_{0.1}O_{2-\delta}$| $Ce_{0.9}Gd_{0.1}O_{2-\delta}$|$La_{0.6}Sr_{0.4}CoO_{3-\delta}$ single cell, anode supported Ni-$Ce_{0.9}Gd_{0.1}O_{2-\delta}$| $Zr_{0.94}Sc_{0.06}O_{2-\delta}$-$Ce_{0.9}Gd_{0.1}O_{2-\delta}$| $La_{0.6}Sr_{0.4}CoO_{3-\delta}$ single cell, and electrolyte supported $La_{0.7}Sr_{0.3}VO_{3-\delta}$-$Ce_{0.85}Sm_{0.15}O_{2-\delta}$|$Ce_{0.85}Sm_{0.15}O_{2-\delta}$|$Ce_{0.85}Sm_{0.15}O_{2-\delta}$-$La_{0.8}Sr_{0.2}CoO_{3-\delta}$ single cell. The microstructure of the supportive Ni-$Ce_{0.9}Gd_{0.1}O_{2-\delta}$ cermet anode and thin $La_{0.7}Sr_{0.3}VO_{3-\delta}$-$Ce_{0.85}Sm_{0.15}O_{2-\delta}$ cermet anode was optimized. The single cells were electrochemically tested using cyclic voltammetry and electrochemical impedance spectroscopy. Various methods, for example scanning electron microscopy and X-ray diffraction, were used for physical characterization of the electrodes.

The analysis of the differences in impedance spectra was applied to determine the cathodic and anodic processes for Ni-$Ce_{0.9}Gd_{0.1}O_{2-\delta}$ anode containing single cells. At higher frequencies probably the dissoactive adsorption of H_2 and transport to the three-phase boundaries, and also the gas diffusion limit the anodic processes while overlapping with dissoactive adsorption of O_2 at the cathode side. At low frequency region, fuel conversion and/or H_2O desorption at microporous Ni-catalytic sites at the anode and electrochemical reduction and transfer of oxygen species to the three-phase boundaries at the cathode are the limiting stages.

It was established that the macro-meso-porous structure and electrochemical activity of supporting Ni-$Ce_{0.9}Gd_{0.1}O_{2-\delta}$ anode depends noticeably on the amount of the pore former added into the raw anode material. However, the electrochemical activity and power density was practically independent of the particle size distribution of the pore former used. Highest power density values have been achieved for anodes with the 4 wt% pore former (with the smallest particle size) in raw anode powder (calculated porosity for non-reduced NiO-$Ce_{0.9}Gd_{0.1}O_{2-\delta}$ was 13.5% but total porosity for reduced sample was 40.7%). The analysis of the difference in impedance spectra showed that the low frequency range depends on both the pore former amount and particle size distribution in the raw anode material while the medium frequency range is more influenced by the pore former particle size distribution.

The best electrochemical performance was reported in the case of ceramic $La_{0.7}Sr_{0.3}VO_{3-\delta}$-$Ce_{0.85}Sm_{0.15}O_{2-\delta}$ anode activated wit CeO_2 and Pd nanoparticles which were proved to be the promising alternatives to Ni-based SOFC anodes. Good electrochemical activity towards both hydrogen and methane oxidation reactions was observed already at 873 K prior to the anode microstructure optimization with the maximum power density of 139 mW cm^{-2} for humidified hydrogen and 101 mW cm^{-2} for humidified methane as a fuel. After the optimization of the anode microstructure the maximum power density increased to 320 mW cm^{-2} for humidified hydrogen and to 175 mW cm^{-2} in the case of humidified methane.

8. REFERENCES

[1] M.C. Williams, J.P. Stzakey, S.C. Singhal, J. Power Sources 131 (2004) 79–85.
[2] E.D. Wachsman, S.C. Singhal, Electrochem. Soc. Interface, 18 (2009) 38–43.
[3] S.C. Singhal, R. Kendall, High Temperature Solid Oxide Fuel Cells: Fundametnal, Design and Application, Elsevier, Amsterdam 2003.
[4] E.D. Wachsman, K.T. Lee, Science 334 (2011) 935–939.
[5] N.G. Minh, T. Takahashi, Science and Technology of Ceramic Fuel Cells, Elsevier, Amsterdam 1995.
[6] B.C.H. Steele, Solid State Ionics, 129 (2000) 95–110.
[7] J.T.S. Irvine, P. Connor, Solid Oxide Fuel Cells: Facts and Figures, Springer, London 2013.
[8] V.V. Kharton, F.M.B. Marques, A. Atkinson, Solid State Ionics 174 (2004) 135–149.
[9] A.S. Nesaraj, J. Sci. Ind. Res. India 69 (2010) 169–176.
[10] E.P. Murray, S.A. Barnett, Solid State Ionics 143 (2001) 265–273.
[11] E. Lust, G. Nurk, S. Kallip, I. Kivi, P. Möller, J. Solid State Electr. 9 (2005) 674–683.
[12] R. Küngas, F. Bidrawn, E. Mahmoud, J.M. Vohs, R.J. Gorte, Solid State Ionics 225 (2012) 146–150.
[13] R. Küngas, F. Birdrawn, J.M. Vohs, R.J. Gorte, Electrochem. Solid-State Lett. 13 (2010) B87–B90.
[14] E. Lust. P. Möller, I. Kivi, G. Nurk. S. Kallip. P. Nigu, K. Lust, J. Electrochem. Soc. 152 (2005) A2306–A2308.
[15] E. Lust, P. Möller, I. Kivi, G. Nurk, S. Kallip, J. Solid State Electrochem. 9 (2005) 88–889.
[16] I.Kivi, P. Möller, H. Kurig, S. Kallip, G. Nurk, E. Lust, Electrochem. Commun. 10 (2008) 1455–1458.
[17] A.J. Samson, P. Hjalmarsson, M. Søgaard, J. Hjelm, N. Bonanos, J. Power Scources 216 (2012) 124–130.
[18] L. Adijanto, R. Küngas, F. Birdrawn, R.J. Gorte, J.M. Vohs, J. Power Sources 196 (2011) 5797–5802.
[19] S. McIntosh, R.J. Gorte, Chem. Rev. 104 (2004) 4845–4865.
[20] M.D. Gross, J.M. Vohs, R.J. Gorte, J. Mater. Chem. 17 (2007) 3071–3077.
[21] H. Kim, C. Lu, W.L. Worrell, J.M. Vohs, R.J. Gorte, J. Electrochem Soc. 149 (2002) A247–A250.
[22] M.L. Toebes, J.H. Bitter, A.J. van Dillen, K.P. de Jong, Catal. Today 76 (2002) 33–42.
[23] S. Helveg, C. Lopez-Cartes, J. Sehested, P.L. Hansen, B.S. Clausen, J.R. Rostrup-Nielsen, F. Abild-Pedersen, J.K. Norskov, Nature 427 (2004) 426–429.
[24] C.W. Sun, U. Stimming, J. Power Sources 171 (2007) 247–260.
[25] J.W. Fergus, Solid State Ionics 177 (2006) 1529–1541.
[26] O.A. Marina, L.R. Pederson, C.A. Coyle, E.C. Thomsen, P. Nachimuthu, D.J. Edwards, J. Power Sources 196 (2011) 4911–4922.
[27] G. Nurk, P. Holtappels, R. Figi, J. Wochele, M. Wellinger, A. Braun, T. Graule, J. Power Sources 196 (2011) 3134–3140.
[28] Y. Matsuzaki, I. Yasuda, Solid State Ionics 132 (2000) 261–269.

[29] G. Nurk, T. Huthwelker, A. Braun, Chr. Ludwig, E. Lust, R.P.W.J. Struis, J. Power Sources 240 (2013) 448–457.
[30] S. Tao, J.T.S. Irvine, Nature Mater. 2 (2003) 320–323.
[31] S. Lee, G. Kim, J.M. Vohs, R.J. Gorte, J. Electrochem. Soc. 155 (2008) B1179–B1183.
[32] J.-S. Park, I.D. Hasson, M.D. Gross, C. Chen, J.M. Vohs, R.J. Gorte, J. Power Sources 196 (2011) 7488–7494.
[33] R.J. Gorte, J.M. Vohs, Curr. Opin. Colloid. In. 14 (2009) 236–244.
[34] S.P.S.Badwal, K. Foger, Ceram. Int. 22 (1996) 257–265
[35] Z. Lu, J. Hardy, J. Templeton, J. Stevenson, J. Power Sources 196 (2011) 39–45.
[36] A.Samson, M. Søgaard, R. Knibbe, N, Bonanos, J. Electrochem. Soc. 158 (2011) B650–B659.
[37] R.N. Basu, A.D. Sharma, A. Dutta, J. Mukhopadhyay, Int. J. Hydrogen Energ. 33 (2008) 5748–5754.
[38] C. Ding, T. Hashida, Energ. Environ. Sci. 3 (2010) 1729–1731.
[39] K. Horiuchi, ECS Trans. 57 (2013) 3–10.
[40] R. Barfod, M. Mogensen, T. Klemensø, A. Hagen, Y.L. Liu, P.V. Hendriksen, J. Electochem. Soc. 154 (2007) B371–B378.
[41] A.Hauch, M. Mogensen, Solid State Ionics 181 (2010) 745–753.
[42] M. D. McIntyre, J. D. Kirtley, D. M. Halat, K. W. Reeping, R. A. Walker, ECS Trans. 57 (2013) 1267–1275.
[43] M. Pihlatie, A. Kaiser, P.H. Larsen, M. Mogensen, J.of Electrochem. Soc. 156 (2009) B322–B329.
[44] T. Klemensø, C. Chung, P.H. Larsen, M. Mogensen, J. of Electrochem. So. 152 (2005) A2186–A2192.
[45] P. Holtappelsa, J.T.S. Irvine, B. Iwanschitz, L.T. Kuhn, L.Y. Lu, Q. Mad, J. Malzbender, A. Mai, T. Ramos, J. Rass-Hansen, B.R. Sudireddy, F. Tietz, V. Vasechko, S. Veltzé, M.C. Verbraeken, ECS Trans. 57 (2013) 1175–1184.
[46] K.B.Yoo, G.M. Choi, Solid State Ionics 192 (2011) 515–518.
[47] A.M. Hussain, J.V.T. Høgh, W. Zhang, E. Stamate, K.T.S. Thydén, N. Bonanos, J. Power Sources 212 (2012) 247–253.
[48] S. Tao, J.T.S. Irvine, Chem. Mater. 16 (2004) 4116–4121.
[49] J.Liu, B.D. Madsen, Z. Ji, S.A. Barnett, Electrochem. Solid-State Lett. 5 (2002) A122–A124.
[50] G. Kim, G. Corre, J.T.S. Irvine, J.M. Vohs, R.J. Gorte, Electrochem. Solid-State Lett. 11 (2008) B16–B19.
[51] B.D. Madsen, S.A. Barnett, Solid State Ionics 176 (2005) 2545–2553.
[52] L. Adijanto, V.B. Padmanabhan, K. Holmes, R.J. Gorte, J.M. Vohs, J. Solid State Chem. 190 (2012) 12–17.
[53] L. Adijanto, V.B. Padmanabhan, R. Küngas, R.J. Gorte, J.M. Vohs, J. Mater. Chem. 22 (2012) 11396–11402.
[54] S. Boulfrad, M. Cassidy, E. Traversa, J.T.S. Irvine, ECS Trans. 57 (2013) 1211–1216.
[55] G. Kim, G. Corre, J.T.S. Irvine, J.M. Vohs, R.J. Gorte, Electrochem. Solid State Letters 11 (2008) B16–B19.
[56] G. Kim, S. Lee, J.Y. Shin, G. Corre, J.T.S. Irvine, J.M. Vohs, R.J. Gorte, Electrochem. Solid-State Lett. 12 (2009) B48–B52.
[57] J.-S. Kim, V.V. Nair, J.M. Vohs, R.J. Gorte, Scripta Mater. 65 (2011) 90–95.

[58] F. Ciucci, W.C. Chueh, D.G. Goodwina, S.M. Haile, PCCP 13 (2011) 2121–2146.
[59] W.C. Chueh, Y. Hao, W.C. Jung, S.M. Haile, Nature Mater.11 (2012) 155–161.
[60] A.Sanson, P. Pinasco, E. Roncari, J. Eur. Ceram. Soc. 28 (2008) 1221–1226.
[61] J. Hu, Z. Lü, K. Chen, X. Huang, N. Ai, X. Du, C. Fu, J. Wang, W. Su, J. Membrane Sci. 318 (2008) 445–451.
[62] P. Holtappels, C. Sorof, M.C. Verbraeken, S. Rambert, U. Vogt, Fuel Cells 2 (2006) 113–116.
[63] R.M.C. Clemmer, S.F. Corbin, Solid State Ionics 180 (2009) 721–730.
[64] R.M.C. Clemmer, S.F. Corbin, Solid State Ionics 166 (2004) 251–259.
[65] F. Zhao, A.V. Virkar, J. Power Sources 141 (2005) 79–95.
[66] J.J. Haslam, A. Pham, B.W. Chung, J.F. DiCarlo, R.S. Glass, J. Am. Ceram. Soc. 88 (2005) 513–518.
[67] L. Holzer, B. Münch, B. Iwanschitz, M. Cantoni, Th. Hocker, Th. Graule, J. Power Sources 196 (2011) 7076–7089.
[68] W. Pan, Z, Lü, K, Chen, X. Huang, B. Wei, W. Li, Z. Wang, W, Su, Electrochimica Acta 55 (2010) 5538–5544.
[69] R.J. Gorte, S. Park, J.M. Vohs, C. Wang, Adv. Mater.12 (2000) 1465–1469.
[70] J.M. Vohs, R.J. Gorte, Adv. Mater. 21 (2009) 943–956.
[71] H.P. He, Y.Y. Huang, J. Regal, M. Boaro, J.M. Vohs, R.J. Gorte, J. Am. Cer. Soc. 87 (2004) 331–336.
[72] S.F. Corbin, P.S. Apté, J. Am. Cer. Soc. 86 (1999) 1693–1701.
[73] R. Küngas, J.-S. Kim, J.M. Vohs, R.J. Gorte, J. Am. Cer. Soc. 94 (2011) 2220–2224.
[74] M. Boaro, J.M. Vohs, R.J. Gorte, J. Am. Cer. Soc. 86 (2003) 395–400.
[75] A. Kossoy, M. Greenberg, K. Gartsman, I. Lubomirsky, J. Electrochem. Soc. 152 (2005) C65–C66.
[76] J.L.M. Rupp, U.P. Muecke, P.C. Nalam, L.J. Gauckler, J. Power Sources 195 (2010) 2669–2676.
[77] J-M. Bae, B.C.H. Steele, Solid State Ionics 106 (1998) 247–253.
[78] A. A. Bieberle-Huetter, P. Reinhard, J.M.L. Rupp, L.J. Gauckler, J. Power Sources 196 (2011) 6070–6078.
[79] X. Zhang, M. Robertson, C. Decès-Petit, Y. Xie, R. Hui, S. Yick, E. Styles, J. Roller, O. Kesler, R. Maric, D. Ghosh, J.Power Sources 161 (2006) 301–307.
[80] T. Matsui, T. Kosaka, M. Inaba, A. Mineshige, Z. Ogumi, Solid State Ionics 176 (2005) 663–666.
[81] X. Zhang, M. Robertson, C. Decès-Petit, Y. Xie, R. Hui, S. Yick, E. Styles, J. Roller, O. Kesler, R. Maric, D. Ghosh, J.Power Sources 161 (2006) 301–307.
[82] T. Horita, K. Yamaji, N. Sakai, H. Yokokawa, A. Weber, E. Ivers-Tiffée, Electrochimica Acta 46 (2001) 1837–1845.
[83] M. Backhaus-Ricoult, Solid State Sciences 10 (2007) 670–688.
[84] F. Bidrawn, R. Küngas, J.M. Vohs, R.J. Gorte, J. Electrochem. Soc. 158 (2011) B514–B525.
[85] R.E. Williford, L.A. Chick, G.D. Maupin, S.P. Simner, J.W. Stevenson, J. Electrochem. Soc. 150 (8) (2003) A1067–A1072.
[86] E. Barsoukov, J.R. Macdonald, Impedance Spectroscopy. Theory, Experiment and Applications, John Wiley, Hoboken 2005.

[87] N. D. Cogger, N. J. Evans, An Introduction to electrochemical impedance measurement, Technical report number 6, Solartron Analytical, Farnborough, England 1999.
[88] C. Xia, W. Rauch, F. Chen, M. Liu, Solid State Ionics 149 (2002) 11–19.
[89] S. Zha, W. Rauch, M. Liu, Solid State Ionics 166 (2004) 241–250.
[90] J. Jamnik, J. Maier, J.Electrochem. Soc. 146 (1999) 4183–4188.
[91] W. Lai, S.M. Haile, PCCP 10 (2008) 865–883.
[92] R. Barford, M. Mogensen, T. Klemensø, A. Hagen, Y.L. Liu, P.V. Henriksen, J. Electrochem. Soc. 154 (2007) B371–B378.
[93] S.H. Jensen, A. Hauch, P.V. Hendriksen, M. Mogensen, N. Bonanos, T. Jacobsen, J. Electrochem. Soc. 145(4) (2007) B1325–B1330.
[94] R. Küngas, I. Kivi, K. Lust, G. Nurk, E. Lust, J. Electroanal. Chem. 630 (2009) 94–101.
[95] S. Primdahl, M. Mogensen, J. Electrochem. Soc. 144 (1997) 3409–3419.
[96] M. Mogensen, K.V. Jensen, M.J. Jorgensen, S. Primdahl, Solid State Ionics 150 (2002) 123–129.
[97] S.Primdahl, M. Mogensen, J. Electochem. Soc. 146, (1999) 2827–2833.
[98] S.Primdahl, M. Mogensen, J. Electochem. Soc. 145 (1998) 2431–2438.
[99] R. Küngas, I. Kivi, E. Lust, J. Electrochem. Soc. 156 (2009) B345–B352.
[100] http://www.solartronanalytical.com/Material-Test-Systems/Model-1260A-Impedance-Gain-phase-Analyzer.aspx last downloaded 21.10.2013
[101] http://www.bronkhorst.com/en/products/gas_flow_meters_and_controllers/elflow_select/ last downloaded 21.10.2013

9. SUMMARY IN ESTONIAN

Mikro-mesopoorsete anoodmaterjalide süntees ja karakteriseerimine ning keskmise temperatuursete tahkeoksiidsete kütuseelementide testimine

Antud doktoritöö raames valmistati erineva disaini ja koostisega tahkeoksiidse kütuseelemendi ühikrakud: elektrolüüt-toetatud Ni-$Ce_{0.9}Gd_{0.1}O_{2-\delta}$|$Ce_{0.9}Gd_{0.1}O_{2-\delta}$|$La_{0.6}Sr_{0.4}CoO_{3-\delta}$ ühikrakk, anood-toetatud Ni-$Ce_{0.9}Gd_{0.1}O_{2-\delta}$|$Zr_{0.94}Sc_{0.06}O_{2-\delta}$-$Ce_{0.9}Gd_{0.1}O_{2-\delta}$|$La_{0.6}Sr_{0.4}CoO_{3-\delta}$ ühikrakk, ja elektrolüüt-toetatud $La_{0.7}Sr_{0.3}VO_{3-\delta}$-$Ce_{0.85}Sm_{0.15}O_{2-\delta}$|$Ce_{0.85}Sm_{0.15}O_{2-\delta}$|$Ce_{0.85}Sm_{0.15}O_{2-\delta}$-$La_{0.8}Sr_{0.2}CoO_{3-\delta}$ ühikrakk. Lisaks optimeeriti toetava Ni-$Ce_{0.9}Gd_{0.1}O_{2-\delta}$ anoodi ja õhukese $La_{0.7}Sr_{0.3}VO_{3-\delta}$-$Ce_{0.85}Sm_{0.15}O_{2-\delta}$ anoodi mikrostruktuuri. Ühikrakkude elektrokeemiliseks karakteriseerimiseks kasutati tsüklilise voltamperomeetria ja elektrokeemilise impedatsspektroskoopia meetodeid ning füüsikaliseks iseloomustamiseks näiteks skaneeriv elektroonmikroskoopia meetodit ja fokuseeriva ioonkiirega skaneerivat eletronmikroskoopiat.

Ni-$Ce_{0.9}Gd_{0.1}O_{2-\delta}$ komposiitanoodi sisaldavate ühikrakkude anood- ja katoodprotsesside määramiseks rakendati uudset meetodit, impendantsspektroskoopia spektrites leiduvate erinevuste analüüsi. Kõrgsageduslikus alas on tõenäoliselt limiteerivaks anoodprotsessiks H_2 dissotsiatiivne adsorptsioon ja transport kolme faasi piirpinnale ja limiteerivaks katoodiprotsessiks O_2 adsoprtsioon. Madalsageduslikus alas limiteeris anoodil kütuse ülekanne ja/või H_2O desorptsioon mikropoorsetele katalüütiliselt aktiivsetele Ni pindadele. Võrreldava kiirusega toimus ka katoodil hapnikuosakeste elektrokeemiline redutseerumine ja transport kolme faasi puutepunktidesse.

Leiti, et toetava Ni-$Ce_{0.9}Gd_{0.1}O_{2-\delta}$ anoodi poorimoodustaja hulk anoodi lähtematerjalides mõjutas märgatavalt anoodi makro-mesopoorset struktuuri ja ühikraku elektrokeemilist aktiivsust, samas kui sõltuvus poorimoodustaja osakese suurusest anoodi elektrokeemilisele aktiivsusele puudus. Kõrgeim maksimaalne võimsustihedus mõõdeti ühikrakul, mille anoodi poorsus oli 40.7% (poorimoodustajana oli anoodi lähtematerjalide segule lisatud 4% väikseima osakese suurusega grafiiti). Samuti leiti, et impedantsspektroskoopia kesksageduslikku piirkonda mõjutas põhiliselt poorimoodustaja hulk anoodi lähtematerjalide segus, samas kui madalsageduslikku ala mõjutas lisaks poorimoodustaja hulgale ka poorimoodustaja osakese suurus anoodi lähtematerjalide segus.

Keraamiline $La_{0.7}Sr_{0.3}VO_{3-\delta}$-$Ce_{0.85}Sm_{0.15}O_{2-\delta}$ anood (aktiveeritud CeO_2 ja Pd nanoosakestega) on uuritud anoodidest kõige kõrgema elektrokeemilise aktiivsusega juba enne keraamilise anoodi mikrostruktuuri optimeerimist. Ühikraku maksimaalne võimsustihedus temperatuuril 873 K ja niisutatud vesiniku keskkonnas oli 139 mW cm^{-2} ja niisutatud metaani keskkonnas 101 mW cm^{-2}. Maksimaalne võimsustihedus niisutatud vesiniku keskkonnas pärast keraamilise anoodi mikrostruktuuri optimeerimist tõusis 320 mW cm^{-2}-ni ja niisutatud metaani keskkonnas 175 mW cm^{-2}-ni.

11. PUBLICATIONS

CURRICULUM VITAE

Name: Kadi Tamm
Date of birth: April 15, 1985
Citizenship: Estonian
Contact: Institute of Chemistry, University of Tartu
Ravila 14a, 50411, Tartu, Estonia
E-mail: k.ktamm@gmail.com

Education:

2009–…	University of Tartu, Institute of Chemistry, PhD student
2009–2011	University of Tartu – Master's degree in teacher of chemistry
2007–2009	University of Tartu – Master's degree in materials science (*cum laude*)
2004–2007	University of Tartu – Bachelor degree in materials science

Professional Employment:

2007–…	University of Tartu, Institute of Chemistry, Chemist

List of publications:

1. E. Lust, I. Kivi, R. Küngas, K. Tamm, P. Möller, A. Sammussenko, E. Anderson, H. Kurig, G. Nurk, Medium temperature solid oxide fuel cells based on the micro-meso-macro-porous cathodes and anodes, ECS Transactions 25 (2009) 325–333.
2. E. Lust, R. Küngas, I. Kivi, H. Kurig, P. Möller, E. Anderson, K. Lust, K. Tamm, A. Samusshenko, G. Nurk, Electrochemical and gas phase parameters of cathodes for intermediate temperature solid oxide fuel cells, Electrochimica Acta 55 (26) (2010) 7669–7678.
3. K. Tamm, I. Kivi, E. Anderson, P. Möller, G. Nurk, E. Lust, Optimization of solid oxide fuel cell Ni-CGO anode porosity, ECS Transaction 35 (1) (2011) 1771–1779.
4. E. Lust, I. Kivi, K. Tamm, P. Möller, E. Anderson, H. Kurig, M. Vestli, G. Nurk, Medium Temperature Solid oxide fuel cells based on supporting porous anode and bilayered electrolyte, ECS Transaction 35(1) (2011) 333–342.
5. I. Kivi, I. Drovtar, E. Anderson, J. Aruväli, K. Tamm, G. Nurk, P. Möller, M. Vestli. R. Kanarbik, E. Lust, Influence of cathode thickness on the oxygen reduction kinetics at the intermediate temperature SOFC cathodes, ECS Transaction 35(1) (2011)2349–2355.
6. R. Kanarbik, P. Möller, I. Kivi, K. Tamm, E. Lust, Development of purification methods of rare earth compounds for preparation of more cost effective solid oxide fuel cell cathodes, ECS Transactions 35(1) (2011) 2227–2232.

7. K. Tamm, I. Kivi, E. Anderson, P. Möller, G. Nurk, E. Lust, Influence of graphite pore forming agents on the structural and electrochemical properties of porous Ni-CGO anode. Journal of the Electrochemical Society 159 (12) (2012) F849–F857.
8. K. Tamm, R. Küngas, R.J. Gorte, E. Lust, Solid oxide fuel cell anodes prepared by infiltration of strontium doped lanthanum vanadate into doped ceria electrolyte, Electrochimica Acta 106 (2013) 398–405.
9. K. Tamm, R. Raudsepp, R. Kanarbik, P. Möller, G. Nurk, E. Lust, Investigation of microstructure of Sr-doped lanthanum vanadium oxide anode based on SDC electrolyte, ECS Transaction 57(1) (2013) 1185–1191.
10. E. Lust, G. Nurk, P. Möller, I. Kivi, R. Kanarbik, K. Tamm, A. Heinsaar, Devolepment of medium-temperature solid oxide fuel cell materials and single cells in Estonia, ECS Transaction 57(1) (2013) 521–527.

ELULOOKIRJELDUS

Nimi: Kadi Tamm
Sünniaeg: 15. aprill 1985
Kodakondsus: Eesti
kontakt: Keemia Instituut, Tartu Ülikool
Ravila 14a, 50411, Tartu, Eesti
E-post: k.ktamm@gmail.com

Haridus:

2009–…	Tartu Ülikool, Keemia Instituut, doktorant
2009–2011	Tartu Ülikool – Magistrikraad keemiaõpetajas
2007–2009	Tartu Ülikool – Magistrikraad materjaliteaduses (*cum laude*)
2004–2007	Tartu Ülikool – Bakalaureusekraad materjaliteaduses

Teenistuskäik:

2007–…	Tartu Ülikool, Keemia Instituut, keemik

Teaduspublikatsioonid:

1. E. Lust, I. Kivi, R. Küngas, K. Tamm, P. Möller, A. Sammussenko, E. Anderson, H. Kurig, G. Nurk, Medium temperature solid oxide fuel cells based on the micro-meso-macro-porous cathodes and anodes, ECS Transactions 25 (2009) 325–333.
2. E. Lust, R. Küngas, I. Kivi, H. Kurig, P. Möller, E. Anderson, K. Lust, K. Tamm, A. Samusshenko, G. Nurk, Electrochemical and gas phase parameters of cathodes for intermediate temperature solid oxide fuel cells, Electrochimica Acta 55 (26) (2010) 7669–7678.
3. K. Tamm, I. Kivi, E. Anderson, P. Möller, G. Nurk, E. Lust, Optimization of solid oxide fuel cell Ni-CGO anode porosity, ECS Transaction 35 (1) (2011) 1771–1779.
4. E. Lust, I. Kivi, K. Tamm, P. Möller, E. Anderson, H. Kurig, M. Vestli, G. Nurk, Medium Temperature Solid oxide fuel cells based on supporting porous anode and bilayered electrolyte, ECS Transaction 35(1) (2011) 333–342.
5. I. Kivi, I. Drovtar, E. Anderson, J. Aruväli, K. Tamm, G. Nurk, P. Möller, M. Vestli. R. Kanarbik, E. Lust, Influence of cathode thickness on the oxygen reduction kinetics at the intermediate temperature SOFC cathodes, ECS Transaction 35(1) (2011)2349–2355.
6. R. Kanarbik, P. Möller, I. Kivi, K. Tamm, E. Lust, Development of purification methods of rare earth compounds for preparation of more cost effective solid oxide fuel cell cathodes, ECS Transactions 35(1) (2011) 2227–2232.
7. K. Tamm, I. Kivi, E. Anderson, P. Möller, G. Nurk, E. Lust, Influence of graphite pore forming agents on the structural and electrochemical

properties of porous Ni-CGO anode. Journal of the Electrochemical Society 159 (12) (2012) F849–F857.
8. K. Tamm, R. Küngas, R.J. Gorte, E. Lust, Solid oxide fuel cell anodes prepared by infiltration of strontium doped lanthanum vanadate into doped ceria electrolyte, Electrochimica Acta 106 (2013) 398–405.
9. K. Tamm, R. Raudsepp, R. Kanarbik, P. Möller, G. Nurk, E. Lust, Investigation of microstructure of Sr-doped lanthanum vanadium oxide anode based on SDC electrolyte, ECS Transaction 57(1) (2013) 1185–1191.
10. E. Lust, G. Nurk, P. Möller, I. Kivi, R. Kanarbik, K. Tamm, A. Heinsaar, Devolepment of medium-temperature solid oxide fuel cell materials and single cells in Estonia, ECS Transaction 57(1) (2013) 521–527.

DISSERTATIONES CHIMICAE UNIVERSITATIS TARTUENSIS

1. **Toomas Tamm.** Quantum-chemical simulation of solvent effects. Tartu, 1993, 110 p.
2. **Peeter Burk.** Theoretical study of gas-phase acid-base equilibria. Tartu, 1994, 96 p.
3. **Victor Lobanov.** Quantitative structure-property relationships in large descriptor spaces. Tartu, 1995, 135 p.
4. **Vahur Mäemets.** The ^{17}O and ^{1}H nuclear magnetic resonance study of H_2O in individual solvents and its charged clusters in aqueous solutions of electrolytes. Tartu, 1997, 140 p.
5. **Andrus Metsala.** Microcanonical rate constant in nonequilibrium distribution of vibrational energy and in restricted intramolecular vibrational energy redistribution on the basis of slater's theory of unimolecular reactions. Tartu, 1997, 150 p.
6. **Uko Maran.** Quantum-mechanical study of potential energy surfaces in different environments. Tartu, 1997, 137 p.
7. **Alar Jänes.** Adsorption of organic compounds on antimony, bismuth and cadmium electrodes. Tartu, 1998, 219 p.
8. **Kaido Tammeveski.** Oxygen electroreduction on thin platinum films and the electrochemical detection of superoxide anion. Tartu, 1998, 139 p.
9. **Ivo Leito.** Studies of Brønsted acid-base equilibria in water and non-aqueous media. Tartu, 1998, 101 p.
10. **Jaan Leis.** Conformational dynamics and equilibria in amides. Tartu, 1998, 131 p.
11. **Toonika Rinken.** The modelling of amperometric biosensors based on oxidoreductases. Tartu, 2000, 108 p.
12. **Dmitri Panov.** Partially solvated Grignard reagents. Tartu, 2000, 64 p.
13. **Kaja Orupõld.** Treatment and analysis of phenolic wastewater with microorganisms. Tartu, 2000, 123 p.
14. **Jüri Ivask.** Ion Chromatographic determination of major anions and cations in polar ice core. Tartu, 2000, 85 p.
15. **Lauri Vares.** Stereoselective Synthesis of Tetrahydrofuran and Tetrahydropyran Derivatives by Use of Asymmetric Horner-Wadsworth-Emmons and Ring Closure Reactions. Tartu, 2000, 184 p.
16. **Martin Lepiku.** Kinetic aspects of dopamine D_2 receptor interactions with specific ligands. Tartu, 2000, 81 p.
17. **Katrin Sak.** Some aspects of ligand specificity of P2Y receptors. Tartu, 2000, 106 p.
18. **Vello Pällin.** The role of solvation in the formation of iotsitch complexes. Tartu, 2001, 95 p.

19. **Katrin Kollist.** Interactions between polycyclic aromatic compounds and humic substances. Tartu, 2001, 93 p.
20. **Ivar Koppel.** Quantum chemical study of acidity of strong and superstrong Brønsted acids. Tartu, 2001, 104 p.
21. **Viljar Pihl.** The study of the substituent and solvent effects on the acidity of OH and CH acids. Tartu, 2001, 132 p.
22. **Natalia Palm.** Specification of the minimum, sufficient and significant set of descriptors for general description of solvent effects. Tartu, 2001, 134 p.
23. **Sulev Sild.** QSPR/QSAR approaches for complex molecular systems. Tartu, 2001, 134 p.
24. **Ruslan Petrukhin.** Industrial applications of the quantitative structure-property relationships. Tartu, 2001, 162 p.
25. **Boris V. Rogovoy.** Synthesis of (benzotriazolyl)carboximidamides and their application in relations with *N*- and *S*-nucleophyles. Tartu, 2002, 84 p.
26. **Koit Herodes.** Solvent effects on UV-vis absorption spectra of some solvatochromic substances in binary solvent mixtures: the preferential solvation model. Tartu, 2002, 102 p.
27. **Anti Perkson.** Synthesis and characterisation of nanostructured carbon. Tartu, 2002, 152 p.
28. **Ivari Kaljurand.** Self-consistent acidity scales of neutral and cationic Brønsted acids in acetonitrile and tetrahydrofuran. Tartu, 2003, 108 p.
29. **Karmen Lust.** Adsorption of anions on bismuth single crystal electrodes. Tartu, 2003, 128 p.
30. **Mare Piirsalu.** Substituent, temperature and solvent effects on the alkaline hydrolysis of substituted phenyl and alkyl esters of benzoic acid. Tartu, 2003, 156 p.
31. **Meeri Sassian.** Reactions of partially solvated Grignard reagents. Tartu, 2003, 78 p.
32. **Tarmo Tamm.** Quantum chemical modelling of polypyrrole. Tartu, 2003. 100 p.
33. **Erik Teinemaa.** The environmental fate of the particulate matter and organic pollutants from an oil shale power plant. Tartu, 2003. 102 p.
34. **Jaana Tammiku-Taul.** Quantum chemical study of the properties of Grignard reagents. Tartu, 2003. 120 p.
35. **Andre Lomaka.** Biomedical applications of predictive computational chemistry. Tartu, 2003. 132 p.
36. **Kostyantyn Kirichenko.** Benzotriazole – Mediated Carbon–Carbon Bond Formation. Tartu, 2003. 132 p.
37. **Gunnar Nurk.** Adsorption kinetics of some organic compounds on bismuth single crystal electrodes. Tartu, 2003, 170 p.
38. **Mati Arulepp.** Electrochemical characteristics of porous carbon materials and electrical double layer capacitors. Tartu, 2003, 196 p.

39. **Dan Cornel Fara.** QSPR modeling of complexation and distribution of organic compounds. Tartu, 2004, 126 p.
40. **Riina Mahlapuu.** Signalling of galanin and amyloid precursor protein through adenylate cyclase. Tartu, 2004, 124 p.
41. **Mihkel Kerikmäe.** Some luminescent materials for dosimetric applications and physical research. Tartu, 2004, 143 p.
42. **Jaanus Kruusma.** Determination of some important trace metal ions in human blood. Tartu, 2004, 115 p.
43. **Urmas Johanson.** Investigations of the electrochemical properties of polypyrrole modified electrodes. Tartu, 2004, 91 p.
44. **Kaido Sillar.** Computational study of the acid sites in zeolite ZSM-5. Tartu, 2004, 80 p.
45. **Aldo Oras.** Kinetic aspects of dATPαS interaction with $P2Y_1$ receptor. Tartu, 2004, 75 p.
46. **Erik Mölder.** Measurement of the oxygen mass transfer through the air-water interface. Tartu, 2005, 73 p.
47. **Thomas Thomberg.** The kinetics of electroreduction of peroxodisulfate anion on cadmium (0001) single crystal electrode. Tartu, 2005, 95 p.
48. **Olavi Loog.** Aspects of condensations of carbonyl compounds and their imine analogues. Tartu, 2005, 83 p.
49. **Siim Salmar.** Effect of ultrasound on ester hydrolysis in aqueous ethanol. Tartu, 2006, 73 p.
50. **Ain Uustare.** Modulation of signal transduction of heptahelical receptors by other receptors and G proteins. Tartu, 2006, 121 p.
51. **Sergei Yurchenko.** Determination of some carcinogenic contaminants in food. Tartu, 2006, 143 p.
52. **Kaido Tämm.** QSPR modeling of some properties of organic compounds. Tartu, 2006, 67 p.
53. **Olga Tšubrik.** New methods in the synthesis of multisubstituted hydrazines. Tartu. 2006, 183 p.
54. **Lilli Sooväli.** Spectrophotometric measurements and their uncertainty in chemical analysis and dissociation constant measurements. Tartu, 2006, 125 p.
55. **Eve Koort.** Uncertainty estimation of potentiometrically measured ph and pK_a values. Tartu, 2006, 139 p.
56. **Sergei Kopanchuk.** Regulation of ligand binding to melanocortin receptor subtypes. Tartu, 2006, 119 p.
57. **Silvar Kallip.** Surface structure of some bismuth and antimony single crystal electrodes. Tartu, 2006, 107 p.
58. **Kristjan Saal.** Surface silanization and its application in biomolecule coupling. Tartu, 2006, 77 p.
59. **Tanel Tätte.** High viscosity $Sn(OBu)_4$ oligomeric concentrates and their applications in technology. Tartu, 2006, 91 p.

60. **Dimitar Atanasov Dobchev**. Robust QSAR methods for the prediction of properties from molecular structure. Tartu, 2006, 118 p.
61. **Hannes Hagu**. Impact of ultrasound on hydrophobic interactions in solutions. Tartu, 2007, 81 p.
62. **Rutha Jäger.** Electroreduction of peroxodisulfate anion on bismuth electrodes. Tartu, 2007, 142 p.
63. **Kaido Viht.** Immobilizable bisubstrate-analogue inhibitors of basophilic protein kinases: development and application in biosensors. Tartu, 2007, 88 p.
64. **Eva-Ingrid Rõõm.** Acid-base equilibria in nonpolar media. Tartu, 2007, 156 p.
65. **Sven Tamp.** DFT study of the cesium cation containing complexes relevant to the cesium cation binding by the humic acids. Tartu, 2007, 102 p.
66. **Jaak Nerut.** Electroreduction of hexacyanoferrate(III) anion on Cadmium (0001) single crystal electrode. Tartu, 2007, 180 p.
67. **Lauri Jalukse.** Measurement uncertainty estimation in amperometric dissolved oxygen concentration measurement. Tartu, 2007, 112 p.
68. **Aime Lust.** Charge state of dopants and ordered clusters formation in CaF_2:Mn and CaF_2:Eu luminophors. Tartu, 2007, 100 p.
69. **Iiris Kahn**. Quantitative Structure-Activity Relationships of environmentally relevant properties. Tartu, 2007, 98 p.
70. **Mari Reinik.** Nitrates, nitrites, N-nitrosamines and polycyclic aromatic hydrocarbons in food: analytical methods, occurrence and dietary intake. Tartu, 2007, 172 p.
71. **Heili Kasuk.** Thermodynamic parameters and adsorption kinetics of organic compounds forming the compact adsorption layer at Bi single crystal electrodes. Tartu, 2007, 212 p.
72. **Erki Enkvist.** Synthesis of adenosine-peptide conjugates for biological applications. Tartu, 2007, 114 p.
73. **Svetoslav Hristov Slavov**. Biomedical applications of the QSAR approach. Tartu, 2007, 146 p.
74. **Eneli Härk.** Electroreduction of complex cations on electrochemically polished Bi(*hkl*) single crystal electrodes. Tartu, 2008, 158 p.
75. **Priit Möller.** Electrochemical characteristics of some cathodes for medium temperature solid oxide fuel cells, synthesized by solid state reaction technique. Tartu, 2008, 90 p.
76. **Signe Viggor.** Impact of biochemical parameters of genetically different pseudomonads at the degradation of phenolic compounds. Tartu, 2008, 122 p.
77. **Ave Sarapuu.** Electrochemical reduction of oxygen on quinone-modified carbon electrodes and on thin films of platinum and gold. Tartu, 2008, 134 p.
78. **Agnes Kütt.** Studies of acid-base equilibria in non-aqueous media. Tartu, 2008, 198 p.

79. **Rouvim Kadis.** Evaluation of measurement uncertainty in analytical chemistry: related concepts and some points of misinterpretation. Tartu, 2008, 118 p.
80. **Valter Reedo.** Elaboration of IVB group metal oxide structures and their possible applications. Tartu, 2008, 98 p.
81. **Aleksei Kuznetsov.** Allosteric effects in reactions catalyzed by the cAMP-dependent protein kinase catalytic subunit. Tartu, 2009, 133 p.
82. **Aleksei Bredihhin.** Use of mono- and polyanions in the synthesis of multisubstituted hydrazine derivatives. Tartu, 2009, 105 p.
83. **Anu Ploom.** Quantitative structure-reactivity analysis in organosilicon chemistry. Tartu, 2009, 99 p.
84. **Argo Vonk.** Determination of adenosine A_{2A}- and dopamine D_1 receptor-specific modulation of adenylate cyclase activity in rat striatum. Tartu, 2009, 129 p.
85. **Indrek Kivi.** Synthesis and electrochemical characterization of porous cathode materials for intermediate temperature solid oxide fuel cells. Tartu, 2009, 177 p.
86. **Jaanus Eskusson.** Synthesis and characterisation of diamond-like carbon thin films prepared by pulsed laser deposition method. Tartu, 2009, 117 p.
87. **Marko Lätt.** Carbide derived microporous carbon and electrical double layer capacitors. Tartu, 2009, 107 p.
88. **Vladimir Stepanov.** Slow conformational changes in dopamine transporter interaction with its ligands. Tartu, 2009, 103 p.
89. **Aleksander Trummal.** Computational Study of Structural and Solvent Effects on Acidities of Some Brønsted Acids. Tartu, 2009, 103 p.
90. **Eerold Vellemäe.** Applications of mischmetal in organic synthesis. Tartu, 2009, 93 p.
91. **Sven Parkel.** Ligand binding to 5-HT_{1A} receptors and its regulation by Mg^{2+} and Mn^{2+}. Tartu, 2010, 99 p.
92. **Signe Vahur.** Expanding the possibilities of ATR-FT-IR spectroscopy in determination of inorganic pigments. Tartu, 2010, 184 p.
93. **Tavo Romann**. Preparation and surface modification of bismuth thin film, porous, and microelectrodes. Tartu, 2010, 155 p.
94. **Nadežda Aleksejeva.** Electrocatalytic reduction of oxygen on carbon nanotube-based nanocomposite materials. Tartu, 2010, 147 p.
95. **Marko Kullapere.** Electrochemical properties of glassy carbon, nickel and gold electrodes modified with aryl groups. Tartu, 2010, 233 p.
96. **Liis Siinor.** Adsorption kinetics of ions at Bi single crystal planes from aqueous electrolyte solutions and room-temperature ionic liquids. Tartu, 2010, 101 p.
97. **Angela Vaasa.** Development of fluorescence-based kinetic and binding assays for characterization of protein kinases and their inhibitors. Tartu 2010, 101 p.

98. **Indrek Tulp.** Multivariate analysis of chemical and biological properties. Tartu 2010, 105 p.
99. **Aare Selberg.** Evaluation of environmental quality in Northern Estonia by the analysis of leachate. Tartu 2010, 117 p.
100. **Darja Lavõgina.** Development of protein kinase inhibitors based on adenosine analogue-oligoarginine conjugates. Tartu 2010, 248 p.
101. **Laura Herm.** Biochemistry of dopamine D_2 receptors and its association with motivated behaviour. Tartu 2010, 156 p.
102. **Terje Raudsepp.** Influence of dopant anions on the electrochemical properties of polypyrrole films. Tartu 2010, 112 p.
103. **Margus Marandi.** Electroformation of Polypyrrole Films: *In-situ* AFM and STM Study. Tartu 2011, 116 p.
104. **Kairi Kivirand.** Diamine oxidase-based biosensors: construction and working principles. Tartu, 2011, 140 p.
105. **Anneli Kruve.** Matrix effects in liquid-chromatography electrospray mass-spectrometry. Tartu, 2011, 156 p.
106. **Gary Urb.** Assessment of environmental impact of oil shale fly ash from PF and CFB combustion. Tartu, 2011, 108 p.
107. **Nikita Oskolkov.** A novel strategy for peptide-mediated cellular delivery and induction of endosomal escape. Tartu, 2011, 106 p.
108. **Dana Martin.** The QSPR/QSAR approach for the prediction of properties of fullerene derivatives. Tartu, 2011, 98 p.
109. **Säde Viirlaid.** Novel glutathione analogues and their antioxidant activity. Tartu, 2011, 106 p.
110. **Ülis Sõukand.** Simultaneous adsorption of Cd^{2+}, Ni^{2+}, and Pb^{2+} on peat. Tartu, 2011, 124 p.
111. **Lauri Lipping.** The acidity of strong and superstrong Brønsted acids, an outreach for the "limits of growth": a quantum chemical study. Tartu, 2011, 124 p.
112. **Heisi Kurig.** Electrical double-layer capacitors based on ionic liquids as electrolytes. Tartu, 2011, 146 p.
113. **Marje Kasari.** Bisubstrate luminescent probes, optical sensors and affinity adsorbents for measurement of active protein kinases in biological samples. Tartu, 2012, 126 p.
114. **Kalev Takkis.** Virtual screening of chemical databases for bioactive molecules. Tartu, 2012, 122 p.
115. **Ksenija Kisseljova**. Synthesis of aza-β^3-amino acid containing peptides and kinetic study of their phosphorylation by protein kinase A. Tartu, 2012, 104 p.
116. **Riin Rebane.** Advanced method development strategy for derivatization LC/ESI/MS. Tartu, 2012, 184 p.

117. **Vladislav Ivaništšev.** Double layer structure and adsorption kinetics of ions at metal electrodes in room temperature ionic liquids. Tartu, 2012, 128 p.
118. **Irja Helm.** High accuracy gravimetric Winkler method for determination of dissolved oxygen. Tartu, 2012, 139 p.
119. **Karin Kipper.** Fluoroalcohols as Components of LC-ESI-MS Eluents: Usage and Applications. Tartu, 2012, 164 p.
120. **Arno Ratas.** Energy storage and transfer in dosimetric luminescent materials. Tartu, 2012, 163 p.
121. **Reet Reinart-Okugbeni**. Assay systems for characterisation of subtype-selective binding and functional activity of ligands on dopamine receptors. Tartu, 2012, 159 p.
122. **Lauri Sikk.** Computational study of the Sonogashira cross-coupling reaction. Tartu, 2012, 81 p.
123. **Karita Raudkivi.** Neurochemical studies on inter-individual differences in affect-related behaviour of the laboratory rat. Tartu, 2012, 161 p.
124. **Indrek Saar.** Design of GalR2 subtype specific ligands: their role in depression-like behavior and feeding regulation. Tartu, 2013, 126 p.
125. **Ann Laheäär.** Electrochemical characterization of alkali metal salt based non-aqueous electrolytes for supercapacitors. Tartu, 2013, 127 p.
126. **Kerli Tõnurist.** Influence of electrospun separator materials properties on electrochemical performance of electrical double-layer capacitors. Tartu, 2013, 147 p.
127. **Kaija Põhako-Esko.** Novel organic and inorganic ionogels: preparation and characterization. Tartu, 2013, 124 p.
128. **Ivar Kruusenberg.** Electroreduction of oxygen on carbon nanomaterial-based catalysts. Tartu, 2013, 191 p.
129. **Sander Piiskop.** Kinetic effects of ultrasound in aqueous acetonitrile solutions. Tartu, 2013, 95 p.
130. **Ilona Faustova**. Regulatory role of L-type pyruvate kinase N-terminal domain. Tartu, 2013, 109 p.